

Effects of dark matter self-interaction on the evolution of the Sagittarius stream

Connor Hainje

Advised by Professor Mariangela Lisanti

May 2021

Abstract

todo

Contents

1	Lambda-CDM	1
1.1	Evidence for dark matter	1
1.2	Lambda-CDM	3
1.3	Structure formation	6
1.4	Small-scale problems	8
2	Self-interacting dark matter	11
2.1	Introduction	11
2.2	Particle physics models	13
2.2.1	Self-coupled scalar	14
2.2.2	Light mediator	15
2.2.3	Strong interactions	16
2.3	Analytic description with baryons	18
2.4	Self-interaction in simulation	24
3	Sagittarius	28
3.1	Overview	28
3.2	Modern models	31
4	Experimental setup	36
4.1	Pipeline and parameters	36
4.2	Equilibration	39
5	Full infall simulations	46
5.1	Description and initial results	46
5.2	Identifying the Sgr progenitor	50
5.3	Time of closest match	59
5.4	Comparison to stream data	59

Chapter 1

Lambda-CDM

1.1 Evidence for dark matter

In 1932, Jan Oort studied the velocities of stars near the Sun, and he found that the velocities of these stars were systematically larger than expected [1]. From the velocities of stars at a given radius in a galaxy, one can measure the gravitational mass of all objects inside that radius. As such, Oort's velocity findings were really a statement about the mass of the Milky Way. In Oort's own words, these velocities implied that the amount of gravitating matter in the Milky Way must be larger than what one can estimate by simply counting stars, with the latter falling short by roughly 30-50% [2].

The next year, Fritz Zwicky studied velocity dispersions in the Coma galaxy cluster [3, 4]. From his measurements, he found that the velocity dispersions required “10 to 100 times more mass” for the cluster to remain bound than could be accounted for by luminous matter. He concluded that there must be some large source of non-luminous matter present to account for the difference, calling the non-luminous matter “dunkle Materie”, or “dark matter”. This is often cited as the origin of the term.

Over the next few decades, evidence continued to mount for the existence of dark matter. Rotation curves began being considered, first by Babcock in 1939 [5] and Oort in 1940 [6]. In the words of Oort, “the distribution of mass in this object [the M31 galaxy] appears to bear almost no resemblance to that of light.” Studies of globular clusters in the Milky Way indicated that at least two-to-three times as much mass must lie outside the orbit of the Sun as inside [7] (todo add Kunth 1952). Studies of binary galaxies revealed large mass-to-light ratios [8, 9] (todo add van den Bergh 1961). More galaxy clusters were studied, and the trends noted by Zwicky were found to hold generally [10]. This mounting evidence largely took the form of acknowledgement of a large mass-to-light ratio; it was not widely thought that a yet unknown form of matter was responsible.

By the 1970s, however, that would change. This was in large part due to developments on a few different fronts. First, the 1960s and 70s saw new methods for measuring the masses of galaxy clusters. Both X-ray measurements and gravitational lensing first began being used in the 1960s to obtain measurements of the masses of galaxy clusters. These studies independently confirmed the large, non-luminous masses that were indicated by the previous velocity analyses. todo add a citation

Second, the cosmic microwave background was discovered in 1965 (todo add a citation), and found to be remarkably isotropic (to better than a part in 10^4). However, strictly baryonic models of the universe suggest anisotropies in the CMB on the order of $\sim 3 \times 10^{-4}$. If the Universe contained some non-baryonic matter which interacted with photons only gravitationally, however, the predicted anisotropies are revised downward, closer to 10^{-5} , consistent with observation. Dark matter seems to fit this role perfectly. Anisotropies on this scale have been observed by more recent studies, beginning with the COBE satellite in 1992 (todo add citation).

Third, data from rotation curves became quite convincing. Rubin and Ford

published improved optical data from the galaxy M31, the same galaxy studied by Oort in 1940 [11]. They found that, to even farther radii than had been previously considered, the rotation curve did *not* decrease outside the optically bright region of the galaxy, an even stronger indicator of the existence of mass not accounted for by luminous matter. Similarly, Roberts and Rots [12] and Roberts and Whitehurst [13] used measurements of 21cm hydrogen emissions to draw very similar conclusions.

Lastly, 1974 saw two watershed papers by independent research groups, each concluding that galaxies have dark halos. Einasto, Kaasik, and Saar wrote “the mass of galactic coronae halos exceeds the mass of populations of known stars by one order of magnitude, as do the effective dimensions” [14]. Similarly, Ostriker, Peebles, and Yahil wrote “the very large mass-to-light ratio and the very great extent of the spiral galaxies can perhaps most plausibly be understood as due to a giant halo of faint stars” [15]. They also note that the year prior, Ostriker and Peebles had come to a similar conclusion from considerations of stability, finding the traditional disk galaxy model to be unstable without a spherical disk [16].

1.2 Lambda-CDM

Since these discoveries, it has been widely believed among astronomers and cosmologists that non-baryonic dark matter exists, that it comprises large, spherical halos around galaxies, and that it played an integral role in the formation of the structures we can see today. Evidence has become increasingly strong with improved measurements of the anisotropy in the CMB (todo cite someone), improved rotation curves for more galaxies (todo cite someone), and better X-ray and gravitational lensing measurements.

Another major question of the twentieth century which came to be largely settled toward its end was that of the cosmological constant, Λ . This constant

was introduced by Einstein into his theory of general relativity (todo explain why). Physically, this constant can be interpreted as the vacuum energy density of empty space. It is often called “dark energy” for this reason [17]. In the late 1990s, measurements of Type Ia supernovae strongly constrained Λ to be positive, giving empty space a significant, constant vacuum energy [18, 19].

These findings, combined with large amounts of evidence for the Big Bang hypothesis, are all most simply described by the Λ CDM model, sometimes called the standard model of cosmology or the concordance model [20]. The model describes the Universe as consisting of three components—the cosmological constant Λ , cold dark matter (CDM), and standard matter—operating under general relativity and coming from an origination event roughly 14 Gyr ago (the Big Bang). This rather simple model is remarkably successful at explaining the Universe.

Through its inclusion of the Big Bang event, the Λ CDM model gives an explanation for the origin of the CMB. In this model, the CMB is a residual radiation left-over from a period shortly after the Big Bang, where the Universe was hot ($>10,000$ K). As the Universe cooled and structures began to form, the photons from this period began to propagate freely in all directions.

The Λ CDM model also provides a well-tested account of the formation of structures in the Universe [20]. In the early Universe, small gravitational perturbations caused matter to collapse into small structures. These small structures—effectively just perturbations in the mass density of the Universe—created gravitational potential wells, attracting other small structures and assembling together to produce larger ones. This works especially well for describing the distribution of dark matter in the Universe, as small pockets of dark matter converge to form subhalos, halos, and larger. The case for baryonic matter and galaxy formation is more complicated, involving baryonic

processes, gas dynamics, and more, but is also well-explained in the régime of hierarchical structure formation. Simulations of hierarchical structure formation have found that it is able to account well for the observed distribution of structures on the scales of galaxies, galaxy clusters, and larger. The implications of this model of structure formation are considered in more detail in the next section.

In fact, the success of this theory of structure formation serves as reason to believe that dark matter is cold (hence the “C” in Λ CDM). Dark matter being “cold” means that it was non-relativistic at the time of decoupling (the period in the early Universe when matter began to fall out of thermal equilibrium) [21]. By contrast, “hot” dark matter (HDM) would have been relativistic at the time of decoupling. Given these higher velocities, the velocity dispersion of HDM would have been non-negligible (differing from the negligible velocity dispersion of CDM). A finite velocity dispersion, however, would have prevented the dark matter particles from being bound to shallow gravitational potential wells, further preventing the formation of small-scale structures [17]. Thus, HDM fails to form structure.

On its own, Λ CDM is remarkably able to explain most of our observations of the Universe. However, there are a few cosmological problems which have arisen. One is known as the horizon problem [22, 17], which points out the the CMB is, to a high degree, isotropic, indicating that the photons making up this radiation are roughly in thermal equilibrium across the sky. However, this means that regions of the sky which are too far separated to be causally connected have remained in equilibrium. This is not explained by Λ CDM.

Another problem is the flatness problem, which points out that there is potentially a fine-tuning problem with the vanilla Λ CDM model [22, 17]. The Universe as we observe it is approximately flat today, meaning that its curvature is approximately unity. If the curvature were not unity, its deviation

from flatness is expected to grow with time. As such, if the Universe is not flat, it must have been *very* close to unity at early times, meaning that this parameter may need to be “fine-tuned” to achieve a reasonable explanation. The problem is that our model should be able to describe parameters like these *without* fine-tuning.

Combining the Λ CDM model with the theory of cosmic inflation, however, solves both of these problems [22]. Inflation posits that the Big Bang was followed by a period of rapid (exponential!) inflationary expansion. Such a phenomenon would solve the horizon problem, as the whole observable Universe would have originated from a much smaller, thermally-connected region before inflation. It also solves the flatness problem, as inflation would have significantly stretched and flattened any curvature in the Universe, providing a natural explanation for the observed flatness today. In fact, this creates a sort of inverse fine-tuning problem: in this theory, any curvature which is *far* from unity requires fine-tuning.

1.3 Structure formation

As stated above, the Λ CDM model predicts structures to form in the Universe as a result of gravitational perturbations at early times. As expansion slows, the pockets of matter created by these perturbations host small gravitational potential wells, causing nearby matter to collapse inward and the growth of structure to occur. With the majority of matter in the Universe being dark matter, the first structures which occur are pockets of dark matter halos. The halos observable today are the result of the hierarchical combination of smaller halos.

The abundance of these halos can be described by extended Press-Schechter (EPS) theory [23]. This theory is grounded on rather simple assumptions: that one can use a spherical collapse model and that one can extrapolate

from linear perturbation theory even into non-linear regimes. Despite these assumptions, it has been shown to give predictions about the mass spectrum of dark matter halos which are in accord with high-resolution numerical simulations.

The halos themselves can be described as virialized objects with mass

$$M_{\text{vir}} = \frac{4\pi}{3} R_{\text{vir}}^3 \Delta_c \rho_c, \quad (1.1)$$

where R_{vir} is the virial radius, ρ_c is the critical density of the Universe, and Δ_c is the over-density parameter. In this work, we choose to set $\Delta_c = 200$ and thus mark the virial mass and radius as with a subscript 200 instead of “vir”.

The Λ CDM model also provides predictions about the internal structure of these dark matter halos. Dark matter-only N-body simulations were performed as early as 1988 [24], with higher-resolution simulations like [25] and [26] following shortly thereafter. The resulting halos from these simulations were found to agree remarkably well with a *two-power* density profile [27]

$$\rho(r) = \frac{\rho_0}{(r/a)^\alpha (1+r/a)^{\beta-\alpha}}, \quad (1.2)$$

where ρ_0 is a characteristic density for the halo and a is the length scale. Special cases of this model include $(\alpha, \beta) = (1, 4)$, the Hernquist model [28], and $(\alpha, \beta) = (1, 3)$, the NFW model [26, 29]. In general, the NFW model enjoys the most usage as one of the most simple and accurate models of the mass density distribution of smaller halos.

todo Include some figures

todo Maybe include a more complete derivation of enclosed mass, NFW virial mass, hernquist total mass, etc.

The required parameters above, ρ_0 and a , are typically reformulated for the

NFW distribution. In particular, we can take a given virial mass M_{200} , determine the corresponding virial radius R_{200} , and define the halo concentration $c = R_{200}/a$. The characteristic density can be found by integrating the density profile up to R_{200} and setting it equal to M_{200} . In this way, the virial mass and concentration are enough to completely specify the NFW distribution. The result is given by

$$\rho_0 = \frac{M_{200}}{4\pi a^3 f(c)}, \quad f(c) = \log(1 + c) - c/(1 + c). \quad (1.3)$$

As these halos are formed hierarchically from smaller halos, however, it has been found that the dense centers of the subhalos are able to survive the merging process. A direct result of this finding is that dark matter halos today should be full of substructure with satellite subhalos of varying sizes. In fact, simulations have shown that the number of subhalos within a halo is approximately self-similar for host halo mass [23]. While it is difficult to determine a method for identifying and counting these subhalos, it does yield a testable prediction of the small-scale structure of dark matter in the Λ CDM paradigm.

todo Discuss galaxy formation with an eye for how this leads to the missing satellites and too-big-to-fail problems

1.4 Small-scale problems

The theory of structure formation that follows from Λ CDM leads us to a few important results. First, we expect the density distributions of dark matter halos to approximately follow the NFW model, specifically with r^{-1} dependence for small r . Second, we expect rich substructure in massive dark matter halos with predictions for the number of subhalos of varying masses contained within. Third, through galaxy formation and the method

of abundance matching, we obtain predictions about the number and masses of satellite galaxies that should be hosted in galaxies like the Milky Way. These three key deductions form the basis for the three classic **small-scale problems** in the Λ CDM model.

The first problem we will discuss is known as the **core-cusp problem**, which is primarily related to the first deduction above. Dark matter-only simulations of CDM halos show that the expected distribution of mass follows a density distribution that is very dense and *cuspy*, i.e. one that goes like r^{-1} at small radii (Bullock and Boylan-Kolchin 2017). As early as 1993, however, it was pointed out that such a distribution is inconsistent with observational data. In particular, “[cuspy] density profiles are excluded by gravitational lensing analyses on cluster scales and by the rotation curves of gas-rich, halo-dominated dwarf spirals on small scales” [30]. It was also recognized by Navarro, Frenk, and White, who wrote “CDM halos are too concentrated to be consistent with the halo parameters inferred for dwarf irregulars” [26].

The second problem is the **missing satellites** problem. Λ CDM simulations predict that galaxies as large as the Milky Way should have as many as $\sim 1\,000$ dark subhalos large enough to host dwarf galaxies [23]. However, as of 2019, less than 60 dwarf galaxies are known within the Milky Way [31].

There exists a potential solution to the missing satellites problem, however, in the form of abundance matching. First, one can expect that dark matter halos become less efficient at making galaxies with decreasing mass, and therefore there exists some threshold mass below which these halos remain completely dark. Then, abundance matching allows one to “solve” the missing satellites problem for the subhalos above this threshold [23].

This solution to the missing satellites problem thus makes a testable prediction. The central masses of Milky Way satellites should be consistent with the central masses of the most massive subhalos in Λ CDM simulation [23].

First probed by Boylan-Kolchin et al. in 2011 (todo cite), however, this does not hold; the most massive subhalos predicted in simulation are significantly more massive than the most massive satellite galaxies. If these subhalos do exist but have just remained dark, then we have a new problem: why did these subhalos fail to form galaxies? This is known as the **too-big-to-fail problem**, as these subhalos ought to be too big to fail to form observable galaxies. If these massive dark subhalos just do not exist, then this is a fundamental failing of the Λ CDM model’s predictions in line with the missing satellites problem.

Some believe that these small-scale problems are the result of the omission of baryonic effects in Λ CDM simulations. As described above, the majority of the conflicting predictions come as the result of dark matter-only simulations. Further, in recent years, it has been shown that all of the above problems (and other small-scale issues) can be reduced or eliminated by the inclusion of stellar feedback and other effects. For example, [32] show that supernova feedback can alleviate the core-cusp problem, and [33] show that stellar feedback can explain the too-big-to-fail problem.

However, prior to these findings, researchers sought modifications to the model that would preserve the successes of Λ CDM on large scales *and* solve the small-scale problems. Some researchers have sought modifications to the model of gravity, but a more popular avenue has been the modification of the dark matter model. While it seems that integration of more sophisticated baryonic processes may be sufficient to solve the small-scale problems, there is no evidence yet that other proposed dark matter models are incorrect descriptions of the particle nature of dark matter. As such, further tests of Λ CDM and these alternative dark matter models are necessary as probes of dark matter particle physics. The alternative dark matter model that we consider in this work is *self-interacting dark matter*, or SIDM.

Chapter 2

Self-interacting dark matter

2.1 Introduction

Self-interacting dark matter (SIDM) was introduced in 2000 by Spergel and Steinhardt [34]. The model was proposed as a solution to the core-cusp and missing satellites problems, as the addition of self-interactions was thought to have three primary effects on the distribution of dark matter.

1. Self-interactions in regions of high density would cause dark matter particles to be unbound, reducing the density of halos primarily in their center region. This would yield a cored density profile rather than a cuspy one, solving the core-cusp problem.
2. It is also expected that interactions would yield a more isotropic velocity dispersion than seen in CDM as well as erase the typical triaxial ellipticity seen in halo shapes. In other words, SIDM halos should be more spherical, a testable prediction.
3. Through the processes of isotropizing the velocity dispersion and reducing density in core regions, it was also expected that substructure

would be greatly reduced, lowering the number of dwarf galaxies and thereby solving the missing satellites problem. However, since the dark matter scattering rate would be naturally dependent on the dark matter density, these effects would only be expected in higher density regions. Toward the outermost radii of halos and on larger scales, the effects of self-interaction would be negligible, preserving the large-scale successes of the Λ CDM model.

One other feature of the model is that the dark matter scattering rate is naturally dependent on the dark matter density. todo finish this thought

Shortly thereafter began a wave of numerical simulations to test these predictions. The results of these simulations were mixed. Some were focused on the evolution of galaxies and found confirmation of the predicted effects (more strongly spherical shape, cored density profile) like [35, 36]. Other simulations, like cluster and cosmological simulations, seemed to show that SIDM would be inconsistent with observation [37, 38, 39].

At the same time, constraints on the allowed self-interaction cross section began being compiled, primarily from clusters. Given the lack of knowledge of the mass of dark matter particles, cross section values are generally given as cross section-to-mass ratios, denoted σ/m . We will use the term cross section interchangeably with this. [40] used cluster simulations to limit the allowable cross section to $< 0.1 \text{ cm}^2/\text{g}$. Similarly, gravitational lensing data from the MS 2137-23 cluster was used by [41] to limit the cross section to $< 10^{-25.5} \text{ cm}^2/\text{GeV}$, approximately $0.02 \text{ cm}^2/\text{g}$. These cross sections were far too small to solve the small-scale problems in galaxies, as simulations like [36] suggested the necessary cross section to be in the range 10^{-25} to $10^{-23} \text{ cm}^2/\text{MeV}$ (0.05 to $5 \text{ cm}^2/\text{g}$).

However, more recent simulations with higher resolution, better statistics, and updated algorithms for considering self-interactions have relaxed many of these constraints significantly, improving the viability of the model and

once again sparking interest in self-interactions. Examples include [42, 43, 44, 45]. These newer, better simulations revised the previous constraints and generally show that cross sections on the order of $\sigma/m \sim 0.1$ to $10 \text{ cm}^2/\text{g}$ are viable and consistent with observation. Of particular relevance for this thesis is [42], which put forth a novel method for computing the effects of self-interactions in N-body simulation. See Subsection 2.4 for a discussion of their method.

[46] have distilled the relevant modern observational constraints on the self-interaction cross section into a table. The data are reproduced in Table 2.1. In particular, notice that the data are consistent with a decaying cross section as the velocity scale increases. Specifically, all data (spiral galaxies and both applications of the too-big-to-fail problem) indicate that the small-scale cross-section ought to be $\gtrsim 0.5$ to $1 \text{ cm}^2/\text{g}$, but the larger-scale cross section ought to be $\sim 0.1 \text{ cm}^2/\text{g}$ or smaller. This rules out any particle models we find with a velocity-independent cross section.

todo add one of those plots that shows it changing slowly for galactic scales

todo add a discussion of what different kinds of astrophysical observations might mean different things about the particle physics properties

2.2 Particle physics models

Given that very little is known conclusively about the particle physics nature of dark matter, the introduction of the possibility of self-interactions makes way for a wealth of rich new theories. We will cover a few of the most popularly considered models below.

	σ/m (cm ² /g)	v_{rel} (km/s)	Observation
Cores in spiral galaxies	$\gtrsim 1$	30-200	Rotation curves
TBTF in Milky Way	$\gtrsim 0.6$	50	Stellar dispersion
TBTF in Local Group	$\gtrsim 0.5$	50	Stellar dispersion
Cores in clusters	~ 0.1	1500	Stellar dispersion, lensing
Halo shape/ellipticity	$\lesssim 1$	1300	Cluster lensing surveys
Substructure mergers	$\lesssim 2$	500-4000	DM-galaxy offset
Merging clusters	$\lesssim \text{few}$	2000-4000	Post-merger halo survival

Table 2.1: Observational constraints on the self-interaction cross section of dark matter. All listed observations are derived from sets of multiple systems. “TBTF” is the abbreviation for “too-big-to-fail.” This is an abridged reproduction of the table compiled by [46]. A distinction is made between “positive observations” (above the horizontal rule) and “constraints” (below the horizontal rule) by the original authors. References to the original papers are given therein.

2.2.1 Self-coupled scalar

The first particle model that we consider is the simplest: a scalar particle, φ , that interacts with itself through a two-to-two coupling. This can be described by the Lagrangian

$$\mathcal{L}_{\text{int}} = -\frac{\lambda}{4!} \varphi^4. \quad (2.1)$$

From the Lagrangian, we can read off the Feynman rule for a four-point intersection to have the matrix element $i\mathcal{M} = -i\lambda$, yielding the two-to-two self-interaction differential cross-section

$$\frac{d\sigma}{d\Omega} = \frac{\lambda^2}{64\pi^2(4m^2)}. \quad (2.2)$$

Integrating over the solid angle and dividing by two to account for identical particles gives a total cross section

$$\sigma(\varphi\varphi \rightarrow \varphi\varphi) = \frac{\lambda^2}{128\pi m^2}. \quad (2.3)$$

One can easily see that this cross section does not admit any kind of velocity independence. Thus, one could make this model consistent for a small subset of scales (e.g. $\sigma/m \sim 1 \text{ cm}^2/\text{g}$ for dwarf galaxy scales), but then it would necessarily fail on other scales. This makes the model viable only for analyses of limited scales where the cross-section is not expected to vary greatly, but it is generally infeasible as a solution to the small-scale problems.

2.2.2 Light mediator

Perhaps the simplest model with a theory rich enough to solve all of the observed problems is one wherein dark matter self-interactions are mediated by a light particle. We will consider a model where dark matter is represented by χ and has mass m_χ , and the mediator field is ϕ with mass m_ϕ . This theory works with both scalar and vector mediators, depending on what specific theory one wants to consider. Perhaps the best motivated origin for such a model is one where the dark matter particle is charged under a spontaneously broken $U(1)$ symmetry and the mediator arises as the corresponding gauge boson [46].

Such a model would have an interaction Lagrangian given by

$$\mathcal{L}_{\text{int}} = \begin{cases} g_\chi \bar{\chi} \gamma^\mu \chi \phi_\mu & (\text{vector mediator}), \\ g_\chi \bar{\chi} \chi & (\text{scalar mediator}), \end{cases} \quad (2.4)$$

where we let the coupling constant be g_χ . In the non-relativistic limit, the

interaction is well-approximated by the Yukawa potential [47, 48]

$$V(r) = \pm \frac{\alpha_\chi}{r} e^{-m_\phi r}, \quad (2.5)$$

where $\alpha_\chi \equiv g_\chi^2/4\pi$ is the dark fine structure constant. The \pm will be set depending on whether the interaction is attractive or repulsive. For a scalar ϕ , the potential is attractive and the sign is $(-)$. For vector ϕ , the potential is attractive $(+)$ for $\chi\bar{\chi}$ scattering and repulsive $(-)$ for $\chi\chi$ and $\bar{\chi}\bar{\chi}$ scattering.

Using the Yukawa potential, we can obtain the Born differential cross section in the limit that $\alpha_\chi m_\chi / m_\phi \ll 1$ to be [46]

$$\frac{d\sigma}{d\Omega} = \frac{\alpha_\chi^2 m_\chi^2}{\left[m_\chi^2 v_{\text{rel}}^2 (1 - \cos \theta)/2 + m_\phi^2\right]^2} \quad (2.6)$$

An important implication of this formula is that the mediator mass must be positive, i.e. $m_\phi > 0$. If instead $m_\phi = 0$, we would then find that $d\sigma/d\Omega \propto v_{\text{rel}}^{-4}$, which is far too strong at small velocities to admit a solution which is consistent with observations. A small but nonzero mediator mass m_ϕ , on the other hand, allows us to “soften” this velocity-dependence to admit a more consistent model.

While quite simple, it has been shown in [48] that it is possible for it to simultaneously accommodate all important observations and solve the small scale problems.

2.2.3 Strong interactions

Some of the richest theories for self-interacting dark matter candidates that one can consider are non-Abelian gauge theories where the dark matter candidates arise as composite bound states. In these theories, the self-interaction manifests as a strong interaction.

The motivation for considering such a model comes from our experience with QCD and the visible sector [49]. For a dark matter model to be a good candidate, it must be stable over the lifetime of the Universe and be neutral under standard model phenomena. Further, we desire models in which the particles exhibit strong self-interactions. These are all properties exhibited by particles in the visible sector under QCD, so it makes sense to consider a similar theory to describe our dark matter candidate. However, we do not necessarily know the gauge group or particle properties of dark matter, leaving us a great freedom to vary the model significantly. Many of the resulting models thus have interesting and unique new physics, though these details are greatly model-dependent.

The primary free parameters of models of this kind are the confinement scale Λ (different from the cosmological constant), and the dark quark mass(es). In the event that our “dark QCD” contains no analogue to electromagnetic/weak interactions, meson-like bound states of the dark quarks could be stable [50]. These mesons can be classified as loosely pion-like, where $m \ll \Lambda$, or quarkonium-like, where $m \gg \Lambda$ [49]. There are several proposed models for each of these scenarios; one of the more well-known is the strongly-interacting massive particle, or SIMP, where the dark matter candidate is pion-like and many non-Abelian theories are possible.

Our non-Abelian model may instead look quite similar to visible QCD, wherein the primary stable bound states are baryonic in nature. In [49], it is noted that the advantage of such models is that “dark matter is automatically sufficiently stable, and no further ultraviolet model-building is needed.” One such dark baryon model is “Stealth Dark Matter,” proposed by the LSD collaboration, which is a scalar dark baryon under a confining $SU(4)$ theory. This theory is named *stealth* dark matter because it is found that the baryons are safe from direct detection, though it does predict a spectrum of lighter meson particles that would be possible to detect at colliders [49].

The third class of candidate particles that has received attention are dark glueballs. Glueballs are bound states of only gluons and are predicted to exist in QCD, but are very difficult to detect. Dark glueballs would then be bound states of dark gluons. Such a model is possible if all the dark fermions in the theory have masses significantly larger than Λ . In this case, glueballs may become stable under an accidental symmetry like baryons, allowing them to be the primary dark matter candidate.

The observables that could result from the above considerations are as diverse as the models themselves. One aspect of these models that we have not considered is what the interactions with the standard model could look like. Some models predict the dark matter candidate to be neutral under standard model interactions, but its constituents to be charged. In such a case, the model would have a coupling to the photon, and it would be possible to directly detect the particle. We may also consider the case where our theory predicts fundamental fermions. It is plausible that these fermions would obtain at least part of their mass through a coupling to the Higgs boson, again providing a mechanism by which we could directly detect the particles. Kribs and Neil provide more details of these observables, as well as collider-specific results, in [49].

2.3 Analytic description with baryons

In 2014, Kaplinghat et al. [51] provided a semi-analytic approach to deriving equilibrium solutions for the dark matter density profile using the Jeans equation. This approach allows for the inclusion of the gravitational potential of both the dark matter and baryons, providing the means to make predictions about the effects of baryons on the dark matter distribution.

The discussion begins with the time-independent Jeans equation, e.g. Equa-

tion 4.209 of [27], which is

$$-\bar{v}_j \frac{\partial(\nu \bar{v}_i)}{\partial r_i} = -\nu \frac{\partial \Phi_{\text{tot}}}{\partial r_j} - \frac{\partial(\nu \sigma_{ij}^2)}{\partial r_j}, \quad (2.7)$$

where ν is the number density of dark matter, $\bar{\mathbf{v}}$ is the mean velocity of dark matter particles, and Φ_{tot} is the total gravitational potential. We assume that the velocity dispersion is a constant σ_0 , and that the time required for dark matter to attain equilibrium through self-scattering is long, which allows us to neglect the self-scattering term (on the left side of the equation). We can also write the equation in terms of the mass density ρ instead of the number density ν , as $\rho \propto \nu$, since each dark matter particle will have the same mass. With these assumptions, the equation becomes

$$\rho \nabla_r \Phi_{\text{tot}}(\mathbf{r}) + \sigma_0^2 \nabla_r \rho(\mathbf{r}) = 0. \quad (2.8)$$

We can divide through by ρ and recognize that $\nabla \rho / \rho = \nabla(\ln \rho)$, yielding

$$\sigma_0^2 \nabla_r (\ln \rho(\mathbf{r})) + \nabla_r \Phi_{\text{tot}}(\mathbf{r}) = 0. \quad (2.9)$$

We then take the derivative of the entire equation. At this point, we can introduce a length scale r_0 and corresponding dimensionless length $\mathbf{x} = \mathbf{r}/r_0$.

$$\sigma_0^2 \nabla_x^2 (\ln \rho(\mathbf{x})) + \nabla_x^2 \Phi_{\text{tot}}(\mathbf{x}) = 0. \quad (2.10)$$

Now we can use Poisson's equation, $\nabla_x^2 \Phi_{\text{tot}}(\mathbf{x}) = r_0^2 \nabla_r^2 \Phi_{\text{tot}}(\mathbf{r}) = 4\pi G r_0^2 \rho_{\text{tot}}(\mathbf{r})$. Letting the dark matter density be ρ and the baryon density be ρ_B , this yields

$$\nabla_x^2 (\ln \rho(\mathbf{x})) + (4\pi G r_0^2 / \sigma_0^2) [\rho_B(\mathbf{x}) + \rho(\mathbf{x})] = 0. \quad (2.11)$$

Now, for convenience, we introduce a function $h(\mathbf{x}) = \ln \rho(\mathbf{x})$ such that

$\rho(\mathbf{x}) = \rho_0 \exp(h(\mathbf{x}))$. The result is given by Equation 1 in [51], here

$$\nabla_x^2 h(\mathbf{x}) + (4\pi G r_0^2 / \sigma_0^2) [\rho_B(\mathbf{x}) + \rho_0 \exp(h(\mathbf{x}))] = 0, \quad (2.12)$$

As a simple test of this equation, we can consider the case where baryonic matter dominates. Then, the $\exp(h)$ term can be neglected, yielding

$$\nabla_x^2 h(\mathbf{x}) + (4\pi G r_0^2 / \sigma_0^2) \rho_B(\mathbf{x}) = 0. \quad (2.13)$$

We use Poisson's equation to rewrite ρ_B in terms of the baryonic gravitational potential Φ_B ,

$$\nabla_x^2 h(\mathbf{x}) + \frac{1}{\sigma_0^2} \nabla_x^2 \Phi_B(\mathbf{x}) = 0. \quad (2.14)$$

Integrating over x gives the solution

$$h(\mathbf{x}) = \frac{1}{\sigma_0^2} (\Phi_B(0) - \Phi_B(\mathbf{x})), \quad (2.15)$$

which corresponds to a dark matter density of

$$\rho(\mathbf{x}) = \rho_0 \exp \left[\frac{1}{\sigma_0^2} (\Phi_B(0) - \Phi_B(\mathbf{x})) \right]. \quad (2.16)$$

The authors then recommend defining the core radius as the radius at which the density is half the initial density, $\rho_0/2$. Such a position would give $h(\mathbf{r}_c) = -\ln 2$, or

$$\Phi_B(0) - \Phi_B(\mathbf{r}_c) = -\sigma_0^2 \ln 2. \quad (2.17)$$

Thus, the core size would depend only on the baryonic potential in the case where it dominates, which follows from these assumptions but stands in marked contrast to observation, where the baryonic contribution does not dominate.

At this point, the authors make the move to consider the spherically sym-

metric case. To do so, they approximate the Milky Way baryon distribution, ρ_B , by a Hernquist profile whose spherical enclosed mass distribution approximates the true enclosed mass distribution. The Hernquist density profile is given by

$$\rho_B(r) = \frac{\rho_{B0}}{(r/r_0)(1+r/r_0)^3}, \quad (2.18)$$

corresponding to a gravitational potential of

$$\Phi_B(r) = -\frac{GM_B}{r+r_0}, \quad (2.19)$$

where M_B is the total mass of baryons in the Milky Way. The free parameters can be set by finding r_0 and $\Phi_B(0)$ such that the circular velocity $V_B(r_0)^2 = -\Phi_B(0)/4$ matches observation. The authors give $\sqrt{-\Phi_B(0)} = 365$ km/s and $r_0 = 2.7$ kpc to be a good fit. We can thus find the core size by solving

$$-\sigma_0^2 \ln 2 = \Phi_B(0) - \Phi_B(r_c) = \Phi_B(0) \left(1 - \frac{1}{1+r_c/r_0}\right), \quad (2.20)$$

which gives

$$r_c \approx \frac{r_0 \sigma_0^2 \ln 2}{-\Phi_B(0)} = \frac{r_0 \sigma_0^2 \ln 2}{4V_B(r_0)^2}. \quad (2.21)$$

For a typical value of σ_0 , on the order of 150 km/s, we thus obtain

$$r_c \approx 0.3 \text{ kpc} \left(\frac{r_0}{2.7 \text{ kpc}}\right) \left(\frac{\sigma_0}{150 \text{ km/s}}\right)^2 \left(\frac{183 \text{ km/s}}{V_B(r_0)}\right)^2, \quad (2.22)$$

which is quite small.

Let's continue under the assumption that the Milky Way is spherically symmetric and that its baryon profile can be approximated by a Hernquist profile, but drop the assumption that baryons dominate the potential. To begin, we will rewrite the Jeans equation in a spherically symmetric system. First, note

that

$$\frac{4\pi Gr_0^2}{\sigma_0^2} \rho_B(x) = \frac{1}{\sigma_0^2} \nabla_x^2 \Phi_B(x) = \nabla_x^2 \left(\frac{\Phi_B(0)}{\sigma_0^2} \frac{1}{1+x} \right). \quad (2.23)$$

Thus, we can rewrite the Jeans equation as

$$0 = \nabla_x^2 \left(h(x) + \frac{\Phi_B(0)}{\sigma_0^2} \frac{1}{1+x} \right) + \frac{4\pi G \rho_0 r_0^2}{\sigma_0^2} e^{h(x)} \quad (2.24)$$

$$= \frac{1}{x^2} \frac{\partial}{\partial x} \left[x^2 \frac{\partial}{\partial x} \left(h(x) + \frac{\Phi_B(0)}{\sigma_0^2} \frac{1}{1+x} \right) \right] + \frac{4\pi G \rho_0 r_0^2}{\sigma_0^2} e^{h(x)}. \quad (2.25)$$

We now introduce a new dimensionless variable, $y = x/(1+x)$. Substituting it in yields

$$\frac{(1-y)^4}{y^2} \frac{\partial}{\partial y} \left[y^2 \frac{\partial}{\partial y} \left(h(y) + \frac{\Phi_B(0)}{\sigma_0^2} (1-y) \right) \right] + \frac{4\pi G \rho_0 r_0^2}{\sigma_0^2} e^{h(y)} = 0. \quad (2.26)$$

Simplifying, we then obtain

$$\frac{1}{y^2} \frac{\partial}{\partial y} \left(y^2 \frac{\partial h}{\partial y} \right) - \frac{2\Phi_B(0)}{\sigma_0^2} \frac{1}{y} + \frac{4\pi G \rho_0 r_0^2}{\sigma_0^2} \frac{e^{h(y)}}{(1-y)^4} = 0. \quad (2.27)$$

The authors recommend that this equation be simplified by letting a_0 be the coefficient for the $\exp(h(y))$ term and $a_1 = -\Phi_B(0)/\sigma_0^2$. The boundary conditions imposed on the equation are then $h(0) = 0$ and $h'(0) = -a_1$, which enforce a core in the center.

We can then solve this equation approximately within the core by approximating the third term by a_0 , equivalent to setting $y = 0$ in this term alone. The resulting equation has approximate solution

$$h(y) \approx -a_1 y - \frac{1}{6} a_0 y^2. \quad (2.28)$$

In the case that baryons dominate, $a_1 \gg a_0$ and the y^2 term becomes negli-

gible. The core radius then is given by the solution to

$$\frac{\ln 2}{a_1} = \frac{r_c}{r_0 + r_c}, \quad (2.29)$$

which is

$$r_c = r_0 \frac{\ln 2}{a_1 - \ln 2} \approx \frac{r_0 \sigma_0^2 \ln 2}{-\Phi_B(0)}, \quad (2.30)$$

the same result as we derived before. In the case that dark matter dominates, $a_0 \gg a_1$ and the y term becomes negligible. The core radius is given by the solution to

$$\frac{6 \ln 2}{a_0} = \left(\frac{r_c}{r_0 + r_c} \right)^2, \quad (2.31)$$

which is

$$r_c = r_0 \frac{\sqrt{6 \ln 2}}{a_0 - \sqrt{6 \ln 2}} \approx r_0 \sqrt{6 \ln 2 / a_0} = \sqrt{\frac{3 \ln 2 \sigma_0^2}{2\pi G \rho_0}}. \quad (2.32)$$

The authors reference an SIDM simulation of a Milky Way-sized halo with a resulting inner density of approximately $2.2 \text{ GeV } c^{-2} \text{ cm}^{-3}$. In the dark matter dominated limit, we thus estimate the core size to be approximately 5.5 kpc, which is consistent with simulation.

For the case where neither baryons nor dark matter dominate, the authors give the following result for the core size

$$r_c \approx r_0 \frac{\sqrt{1 + \frac{2 \ln 2 a_0}{3 a_1^2}} - 1}{1 + \frac{a_0}{3 a_1} - \sqrt{1 + \frac{2 \ln 2 a_0}{3 a_1^2}}}. \quad (2.33)$$

However, we have potentially a family of solutions parameterized by a_0 and a_1 . As a criterion for consistent selection, then, the authors adopt the following convention. Let r_1 be the radius at which the average dark matter particle has undergone one interaction. We choose the values of a_0 and a_1 such that the mass and total energy within r_1 match the values that one would have had in the absence of self-interactions. To compare against “the

absence of self-interactions,” one can look at, for example, an NFW profile that approximately fits the considered galaxy.

For the Milky Way, we can consider the self-interaction cross section required for r_1 to be approximately the solar radius, 8.5 kpc. The local dark matter density is known to be approximately $0.2 \text{ GeV } c^{-2} \text{ cm}^{-3}$. We can also estimate the age of the Milky Way to be 10 Gyr. Thus, we expect the average number of scatterings to be approximately

$$(0.2 \text{ GeV } c^{-2} \text{ cm}^{-3}) (150 \text{ km/s}) (\sigma/m) (10 \text{ Gyr}). \quad (2.34)$$

A self-interaction cross section of about $\sigma/m = 1 \text{ barn/GeV}$ ($0.56 \text{ cm}^2/\text{g}$) sets this to one scattering event per particle. As we have seen, this cross section is consistent with observations on the scales of galaxies and is capable of solving the small-scale problems.

The authors specifically consider values of σ_0 , ρ_0 , and r_1 that approximate the Milky Way in the case that the no-self-interaction halo is well described by an NFW profile. They find that $r_1 = 15 \text{ kpc}$, $\sigma_0 = 165 \text{ kpc}$, $\sigma/m = 1 \text{ barn/GeV}$, and $\rho_0 = 14 \text{ GeV } c^{-2} \text{ cm}^{-3}$ gives a good fit. When plugged into Equation 2.33, this yields an expected core size of 0.43 kpc. The resulting density profiles are shown in Figure 2.1. In particular, note that the dashed red curve (SIDM analog to the standard NFW Milky Way) attains half its central density at approximately 0.5 kpc, in line with the analytic expectation.

2.4 Self-interaction in simulation

In this work, we will be exploring the introduction of self-interaction in predictions about the infall of the Sagittarius dwarf galaxy and, specifically, the formation of its stream. This is done through the use of N-body simulations. As such, we present a description of how these self-interactions are modeled in simulation. We choose to use GIZMO [52] for our simulations, and the

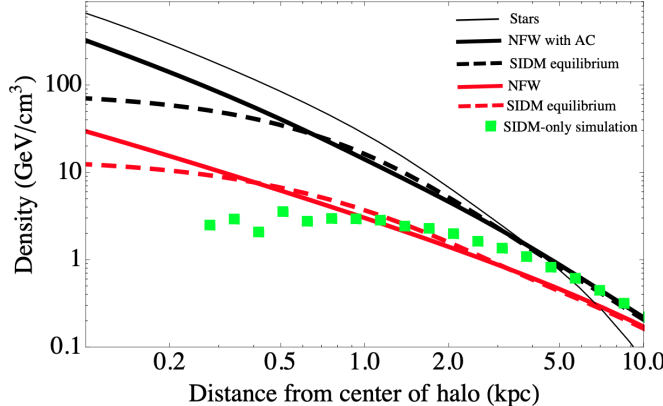


Figure 2.1: Mass density distributions for a Milky Way-sized halo. The green boxes show the result of a dark matter-only SIDM simulation. The thick solid lines show NFW distributions, both adiabatically contracted (black) and not (red). (We focus only on the non-adiabatically contracted case in this study.) The dashed lines show the corresponding analytic SIDM profiles expected from the results of the Jeans equation-based formalism. This figure is reproduced from Figure 1 of [51].

implementation of self-interactions therein is the one described by [42]. Much of the following discussion comes in large part from [42].

In our simulation, we consider some number of “macro-particles,” each of which represents an ensemble of dark matter particles, a patch of the dark matter phase-space density. We let each macro-particle have mass m_p , and we keep this mass consistent across all dark matter macro-particles. Since we consider the macro-particle as representing a patch of the phase-space density, we consider its position to be centered at some point \mathbf{x} but spread out according to a kernel $W(r, h)$. Here, r is the distance from the center of the macro-particle and h is a smoothing length. In GADGET-2, from which

GIZMO is built, the kernel is given by

$$W(r, h) = \frac{8}{\pi h^3} \begin{cases} 1 - 6(r/h)^2 + 6(r/h)^3 & 0 \leq r/h \leq 1/2, \\ 2(1 - r/h)^3 & 1/2 < r/h \leq 1, \\ 0 & r/h > 1. \end{cases} \quad (2.35)$$

todo find whether this is the same for GIZMO. todo find how h is determined in GIZMO. The velocity of the macro-particle, on the other hand, is taken to be a delta function, such that the macro-particles have a single defined velocity.

When the patches represented by two macro-particles overlap, we can compute the interaction rate between them. The rate of scattering of a macro-particle j off a target particle i is given by

$$\Gamma(i|j) = (\sigma/m)m_p|\mathbf{v}_i - \mathbf{v}_j|g_{ji}, \quad (2.36)$$

where σ/m is the familiar cross-section to mass ratio and g_{ij} is a number density factor whose purpose is account for the overlap of the two macro-particles' smoothing kernels. It is given by

$$g_{ji} = \int_0^h d^3\mathbf{x}' W(|\mathbf{x}'|, h) W(|\delta\mathbf{x}_{ji} + \mathbf{x}'|, h), \quad (2.37)$$

with $\delta\mathbf{x}_{ji}$ the displacement vector between the macro-particle positions.

Over the course of a time step δt , the probability of an interaction of macro-particle j off target macro-particle i is given by

$$P(i|j) = \Gamma(i|j) \delta t. \quad (2.38)$$

The total probability of interaction between these two particles in this time

step, then, would be the average of the two directed probabilities, i.e.

$$P_{ij} = \frac{1}{2} (P(i|j) + P(j|i)). \quad (2.39)$$

To actually represent the interaction, then, one draws a random number and adjusts the velocities of the particles if the number lies below the probability. The velocities are adjusted in a manner consistent with an elastic scattering which is isotropic in the center of mass frame.

More details are presented in [42], including the derivation of the scattering rate formula from the Boltzmann equation. We use the implementation which is packaged with the publicly-available GIZMO simulation suite.

Chapter 3

Sagittarius

3.1 Overview

Sagittarius (Sgr) is a dwarf spheroidal (dSph) galaxy in the Milky Way. It was the ninth dwarf satellite discovered in the Milky Way, and the last to be discovered before the advent of digital surveys [31]. It was identified in 1994 by Ibata et al. [53] as a dwarf satellite in the constellation of Sagittarius (hence its name). The authors then noted that it was the closest known galaxy to the Milky Way of any known at the time, and this has largely remained true to the present. One quirk about Sgr that was noted at the time was that it “is elongated towards the plane of the Milky Way, suggesting that it is undergoing some tidal disruption before being absorbed by the Milky Way.” This would turn out to be a very important feature of Sgr to explain.

In the years since, many studies have been performed to try to understand and quantify various properties of Sgr, like its mass, orbital time, and the reason for its elongated shape. By 2000, it was believed that the elongation was the result of tidal shearing [54], meaning that accurately describing the

orbital history of Sgr is essential. Further, this means we can expect that the stripping of stars by tidal forces may play a significant role in its evolution. Jiang and Binney [54] thus explored the parameter space for the initial mass and radius of Sgr, finding that a wide range of parameters are possible, from an initial mass of $\sim 10^{11} M_{\odot}$ and Galactocentric distance of $\gtrsim 200$ kpc to mass $\sim 10^9 M_{\odot}$ and distance ~ 60 kpc.

Shortly thereafter, Majewski et al. used the Two Micron All Sky Survey (2MASS) to map Sgr, forming the first canonical model of Sgr [55]. Their characterization of Sgr included a description of a *stream* of stars that had been tidally stripped from Sagittarius, forming leading and trailing “tidal tails”. These tails, they note, “lie along a well-defined orbital plane about the Galactic center.” Moreover, they state that the lack of precession in the tidal debris is indicative of a nearly spherical gravitational potential for the Milky Way, recognizing the usefulness of the Sagittarius stream as a potential measure of the gravitational potential.

We have included a reproduction of Figure 11 from [55], a plot of a sample of Sgr debris stars in equatorial coordinates and in the orbital plane. It can be seen in Figure 3.1. The core of Sgr lies at approximately $(+20, -10)$ in the orbital coordinates, with the northern arm leading above it and the southern arc leading to the left.

A similar work was performed by Belokurov et al. in 2006, using the Sloan Digital Sky Survey (SDSS) [56]. They found the tidal stream of Sgr to be “clearly visible”, and found the leading tidal arm to be especially clear. We include their Figure 2, which shows a panoramic view of the stream cutting together the 2MASS stars of Majewski et al. with the SDSS stars of Belokurov et al. This can be found in our Figure 3.2.

The picture of Sagittarius as tidally disrupted with debris forming a long streaming arc about the Milky Way would turn out to be well-supported by further observations and studies. In the ensuing years, more studies were

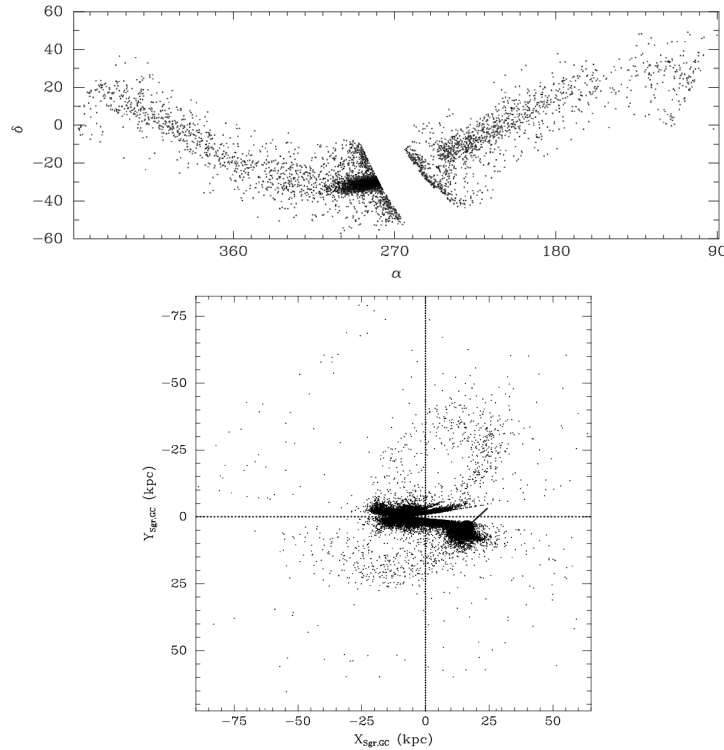


Figure 3.1: Sgr debris in (top) equatorial coordinates and (bottom) in the orbital plane with the Galactic center at the origin. Reproduced from Figure 11 of [55].

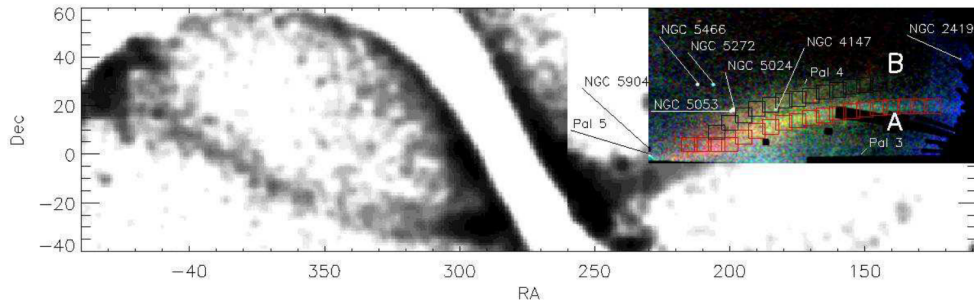


Figure 3.2: Sgr debris in equatorial coordinates, including both the 2MASS data from [55] (in grayscale) as well as SDSS data from [56] (in color). Reproduced from Figure 2 of [56].

performed to improve the model and more accurately quantify the properties of the galaxy. We note in particular the work of Kunder and Chaboyer [57] who estimated the distance to Sgr to be approximate 24.8 kpc.

todo add a discussion of stream coordinates?

3.2 Modern models

The next major discovery in the history of Sagittarius was the 2010 Law and Majewski model [58]. This model became the first two successfully satisfy the majority of existing constraints on the angular position, distance, and radial velocity of the tidal debris streams. It did so using a triaxial Milky Way halo; in other words, it dropped the typical assumption that the Milky Way halo is axisymmetric in the Galactic plane. One prediction of note from this model is that the current bound mass of Sgr is approximately $2.5 \times 10^8 M_\odot$. To obtain this, they use an initial mass of $6.4 \times 10^8 M_\odot$ with an infall orbit for around 8 Gyr in a fixed Galactic gravitational potential. It is worth noting that this initial mass lies in the régime where dynamical friction is small and the effects of tidal stripping on the Sgr progenitor are relatively small [59].

The resulting distribution of stars is shown in Figure 3.3. We reproduce their plots of the debris stream in terms of heliocentric coordinates and Galactocentric distances in the orbital plane. The coloring corresponds to the time at which the debris was stripped from Sgr. (Green is between the first and third apocenters, cyan between the third and fifth, magenta between the fifth and seventh, and orange later than the seventh.) Notice as well that they predict *two* wraps for both the leading (“L”) and trailing (“T”) stream arms.

Shortly thereafter came the model of Purcell et al. [60]. In their model, they explicitly account for the impact of the infall of Sagittarius on the evolution of the Milky Way disk, pointing out that all then-existing models of Sgr

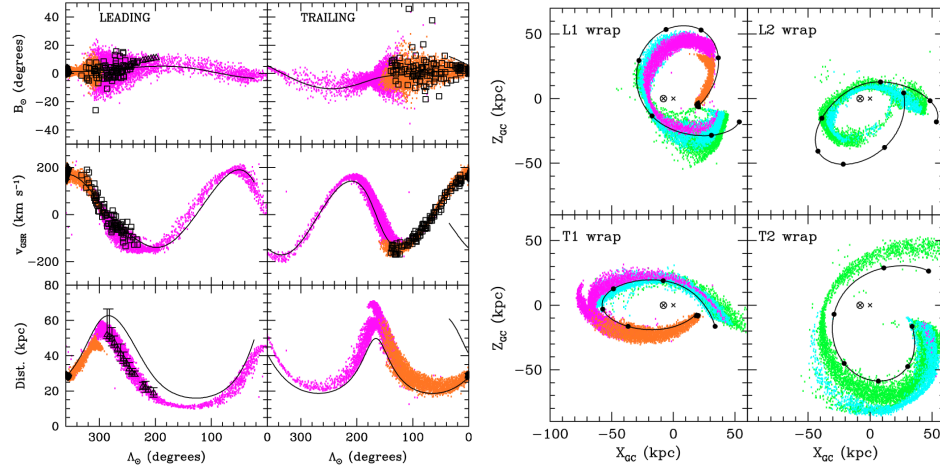


Figure 3.3: Sgr stellar debris streams according to the Law and Majewski 2010 model. On the left, debris stripped in the last ~ 3 Gyr is shown in terms of stream and heliocentric coordinates. On the right, the first two wraps of the leading (“L”) and trailing (“T”) stream arms are shown in the orbital plane. These plots are reproduced from Figures 6 and 8 of [58].

assume that its effects on the Galactic disk morphology are negligible. They found that Sgr created “significant perturbations to the outer disk” with noticeable effects on the evolution of the inner spirality. In their model, Sgr is represented as beginning with halo mass $10^{10.5} M_{\odot}$ at a Galactocentric radius of 80 kpc in the Galactic plane. In order to account for tidal stripping that would have occurred between the infall of Sgr past the MW virial radius and the starting position they choose, they truncate the initial halo at the instantaneous Jacobi radius, $r_t = 23.2$ kpc. We note that such methods may produce qualitatively accurate representations of Sgr but are unlikely to accurately reflect the true orbital history of Sgr.

The resulting stream debris is shown in Figure 3.4. We show again both the stream in terms of heliocentric coordinates and in the orbital plane in terms of Galactocentric distances. We focus in particular on the “light Sgr” subplot of the Galactocentric figure. The figures show qualitatively similar

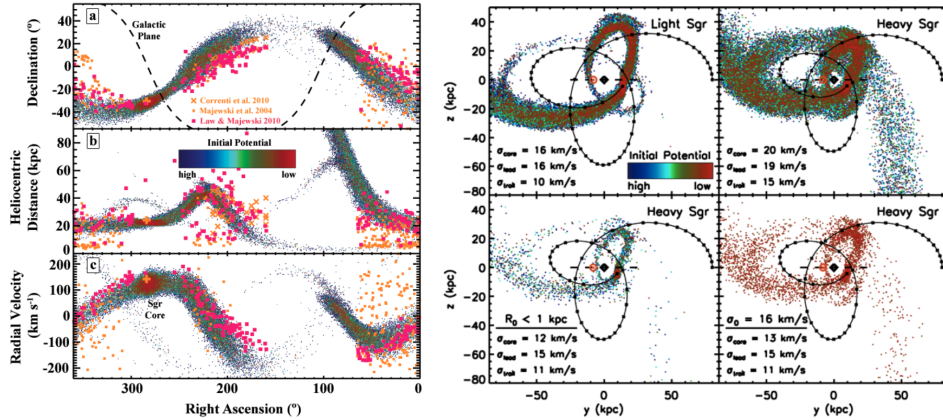


Figure 3.4: Sgr stellar debris streams according to the Purcell et al. 2011 model. On the left, debris is shown in terms of equatorial and heliocentric coordinates. On the right, the debris is shown in terms of Galactocentric distances in the orbital plane. We pay particular attention to the “light Sgr” subplot and note that the debris appears to contain approximately the same shape as the “L1” and “T1” wraps of the Law model. Figures reproduced from Figures 3 and S4 of [60].

patterns to the model of Law and Majewski [58], including the “L1” and “T1” wraps.

As such, the status until quite recently was that no existing Sagittarius model did could accurately account for a live Milky Way potential, the effects of dynamical friction, and the early infall of Sgr at Galactocentric radii of more than 60-80 kpc. In 2017, however, a new model which sought to solve all these problems was found by Dierickx and Loeb [59]. They simulate the infall of Sagittarius starting from its first crossing of the Milky Way virial radius approximately 8 Gyr ago using a live Milky Way gravitational potential and accounting for the full effects of dynamic friction. To find the best-fit model, they began by performing a parameter search with a fast and simple semi-analytic model. They then used these best-fit parameters in a full, high-resolution N-body simulation.

The resulting simulation is able to reproduce both the leading and trailing stream arms to good agreement with both observed data and past models. Moreover, they note that the resulting model is the first to accurately reproduce existing data for debris observed 100 kpc away. The model also predicts the existence of an extension to the stream, including “the existence of several arms of the Sgr stream extending to hundreds of kiloparsecs.” They note that this predicted structure matches the positions of the two most distant stars known in the Milky Way halo and serves as a testable prediction for data from future sky surveys.

This model is the one that we have (approximately) chosen to adopt for our simulations. The specific differences between our model and theirs will be elucidated in (todo add reference to simulation section). Dierickx and Loeb represent the Milky Way halo using a Hernquist distribution with total mass $1.25 \times 10^{12} M_{\odot}$ and scale radius 38.35 kpc. The Milky Way disk follows an exponential profile with mass $8.125 \times 10^{10} M_{\odot}$, scale length 3.5 kpc, and scale height 0.525 kpc. They also use a Hernquist bulge with mass $1.25 \times 10^{10} M_{\odot}$ and scale length 0.7 kpc. In their model, Sagittarius has a Hernquist halo with total mass $1.3 \times 10^{10} M_{\odot}$ and scale radius 9.81 kpc. It has an exponential disk with mass $6 \times 10^8 M_{\odot}$, scale length 0.85 kpc, and scale height 0.1275 kpc, and a Hernquist bulge with mass $5.2 \times 10^8 M_{\odot}$ and scale length 0.17 kpc.

As before, we include plots of the resulting stellar debris, both in terms of heliocentric coordinates and Galactocentric distances in the orbital plane. These plots are given in Figure 3.5. In this case, the familiar stream structure is once again reproduced, but with the inclusion of a significant extension to the stream arms far beyond the two wraps considered by Law and Majewski. The resulting distribution also appears to approximately reproduce the distributions of observed stars (observational data shown in black).

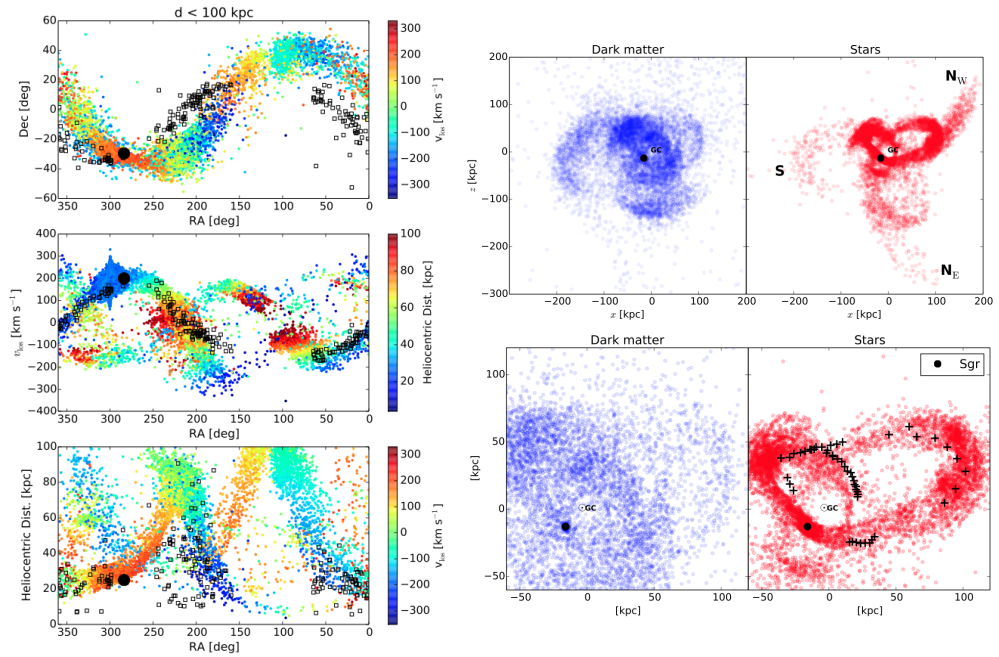


Figure 3.5: Sgr stellar debris according to the Dierickx and Loeb 2017 model. As before, we show the stream in equatorial and heliocentric coordinates on the left. On the right is the stream (and associated dark matter particles) in terms of Galactocentric distances in the orbital plane. The right top subfigure shows the full distributions, while the right bottom subfigure zooms into the more observationally relevant region. Comparisons to observed Sgr stars are also shown in black. Plots reproduced from Figures 8, 9, and 10 of [59].

Chapter 4

Experimental setup

As stated previously, the core work of this thesis is performing N-body simulations of the infall of Sgr in the style of Dierickx et al. [59], varying the initial conditions and dark matter model to determine the resulting impacts on the evolution of the Sgr tidal debris stream. As such, we provide an overview of the setup of the simulations we performed in this section.

4.1 Pipeline and parameters

To begin our experimental pipeline, we first generate the initial distributions of stellar and dark matter particles using a package called GalactICS [61]. Each galaxy is modeled using a stellar disk and dark matter halo. The halo follows a Navarro-Frenk-White (NFW) profile

$$\rho_{\text{halo}}(r) = \frac{M_{200}}{4\pi a^3 f(c)} \frac{1}{(r/a)(1+r/a)^2}, \quad (4.1)$$

where $f(c) = \log(1+c) - c/(1+c)$, M_{200} is the virial mass, a is the scale length, c is the concentration, and $c = r_{200}/a$. Here, we use a lowercase r to denote the radius in a spherical sense.

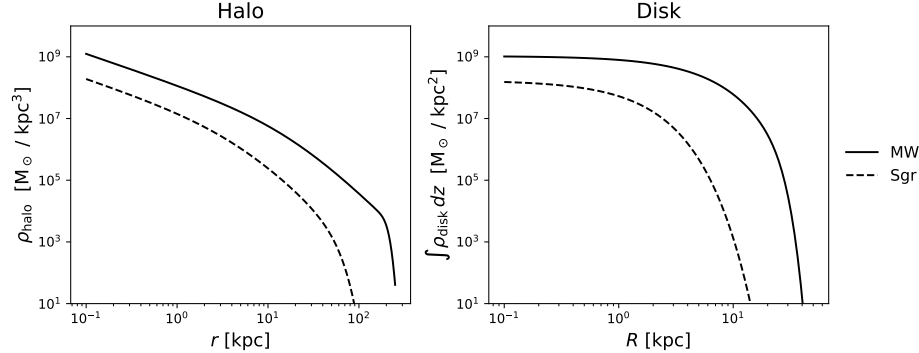


Figure 4.1: Initial profiles for the halo and disk of both galaxies. The halos follow a truncated NFW profile and the disks follow a truncated exponential-sech² profile. Note that the disk density is in cylindrical coordinates and is integrated over the z direction.

The stellar disk follows an exponential-sech² profile, given by

$$\rho_{\text{disk}}(R, z) = \frac{M_{\text{disk}}}{4\pi R_0^2 z_0} \exp(-R/R_0) \operatorname{sech}^2(z/z_0), \quad (4.2)$$

where R_0 is the disk scale length, z_0 is the disk scale height, and the capital R denotes the cylindrical radius in the plane of the disk.

Both of these distributions are subject to truncation beyond a certain radius, r_t , with truncation width dr_t . The truncation function comes from [62] and is given by

$$C(r; r_t, dr_t) = \frac{1}{2} \operatorname{erfc} \left(\frac{r - r_t}{\sqrt{2} dr_t} \right). \quad (4.3)$$

For the halos, the truncation radius is simply the virial radius and the truncation width is 20 kpc. For the disks, the truncation radius is 25 kpc, the width is 5 kpc, and the truncation is only applied to R in the disk plane. The distributions, including the truncation parameter, can be seen in Figure 4.1.

Bundled with GalactICS is a subpackage called GadgetConverters, which

Parameters	MW	Sgr
Halo		
Virial mass	M_{200}	$10^{12} M_\odot$
Virial radius	r_{200}	206 kpc
Concentration	c	10
Particles	N_{halo}	1.16×10^6
Disk		
Mass	M_{disk}	$6.5 \times 10^{10} M_\odot$
Scale length	R_0	3.5 kpc
Scale height	z_0	0.53 kpc
Particles	N_{disk}	2.03×10^6

Table 4.1: Parameters for the initial Milky Way and Sgr galaxies in our full simulation. These values are in large part taken from the work of [59].

provides a pipeline for converting the native output of GalactICS into a binary compatible with GADGET and derivative N-body simulation software. In this work, we use GIZMO [52], which is itself derived from GADGET-2 [63].

The parameters that were used for our simulations were largely taken from the work of Dierickx et al. [59]. They are summarized in Table 4.1. There are a few key differences between their model and our simulations, however. First, they used Hernquist profiles for their halos, while we use NFW distributions. The NFW parameters we use, however, come from their work, where they are given as the parameters which yield an approximately equivalent distribution. A comparison between their Hernquist and our NFW profiles is shown in Figure 4.2; the differences are quite small.

The second source of discrepancy between their work and ours is that we have less resolution in our stellar profile than in their work. This is in part because they used a Hernquist bulge in both their Milky Way and Sgr, wherer this has been omitted from our work. It is also because they used more stellar particles for the Sgr disk than we did (1.94×10^4 versus 1.17×10^4), owing

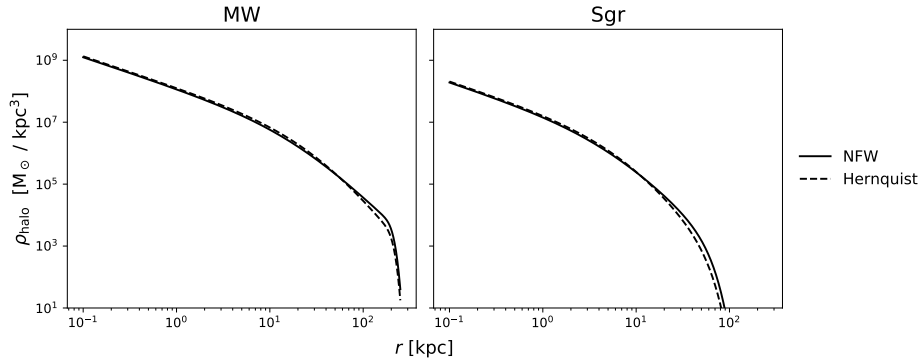


Figure 4.2: Comparison between the density profiles of the relevant truncated NFW and truncated Hernquist profiles for the Milky Way and Sgr galaxies in the Dierickx model. The NFW parameters can be found in Table 4.1. The Hernquist parameters are as follows: total MW halo mass $1.25 \times 10^{12} M_{\odot}$, MW scale radius 38.35 kpc, total Sgr halo mass $1.3 \times 10^{10} M_{\odot}$, Sgr scale radius 9.81 kpc.

to a technical error in our initial conditions creation pipeline.

The experiments performed herein were performed using GIZMO version (todo find out) on Princeton Research Computing’s Della cluster. This cluster is an Intel cluster with ≥ 20 cores per node and ≥ 128 GB memory per node [64]. Our simulations often used around 10 GB of RAM and typically split the computation over 25 cores.

4.2 Equilibration

After generating the initial particle distributions for each galaxy, we evolved each one forward in time for a several Gyr to allow it to equilibrate. For our runs involving SIDM, we perform this equilibration run with SIDM micro-physics turned on, allowing for the creation of a core in the central region of the dark matter halo.

For each galaxy, we begin with the parameters discussed in the previous

section and perform two equilibration runs: one using CDM microphysics and one using SIDM microphysics with a cross section of $\sigma/m = 10 \text{ cm}^2/\text{g}$. In this study, we choose to use a somewhat high cross section in order to exaggerate any differences that may appear because of the presence of self-interaction. We note that future studies should consider a range of cross sections.

For the Milky Way equilibrations—both CDM and SIDM—we only evolve the galaxy forward for 1 Gyr, writing time stamps approximately every 0.1 Gyr. This is because we expect the initial distribution to be relatively close to equilibrium, especially when considering such a large galaxy. The resulting evolution of the mass density profiles are shown in Figure 4.3.

In these plots, we can see that the CDM halo starts in a state which is already close to equilibrium. The halo changes very little, and the disk slowly pulls a small amount of density in toward the center. The SIDM halo, however, almost immediately develops a rather substantial core, which slowly dissolves somewhat, leaving a small core with size $\sim 1 \text{ kpc}$. This is almost certainly because of the disk. As the disk equilibrates, its central density increases, increasing the gravitational potential in the center of the galaxy and counteracting the coring effect of self-interactions.

We can also compare these results to those we might have expected following the analytic formalism for determining the core size in Section 2.3. To begin, we need to find the scale radius r_0 and the center value of the gravitational potential $\Phi_B(0)$ in the “spherical disk” approximation. We can do so by using the following two relations:

$$\Phi_B(0) = -\frac{GM_B}{r_0} \quad (4.4)$$

$$V_B(r_0) = \frac{\sqrt{-\Phi_B(0)}}{2}, \quad (4.5)$$

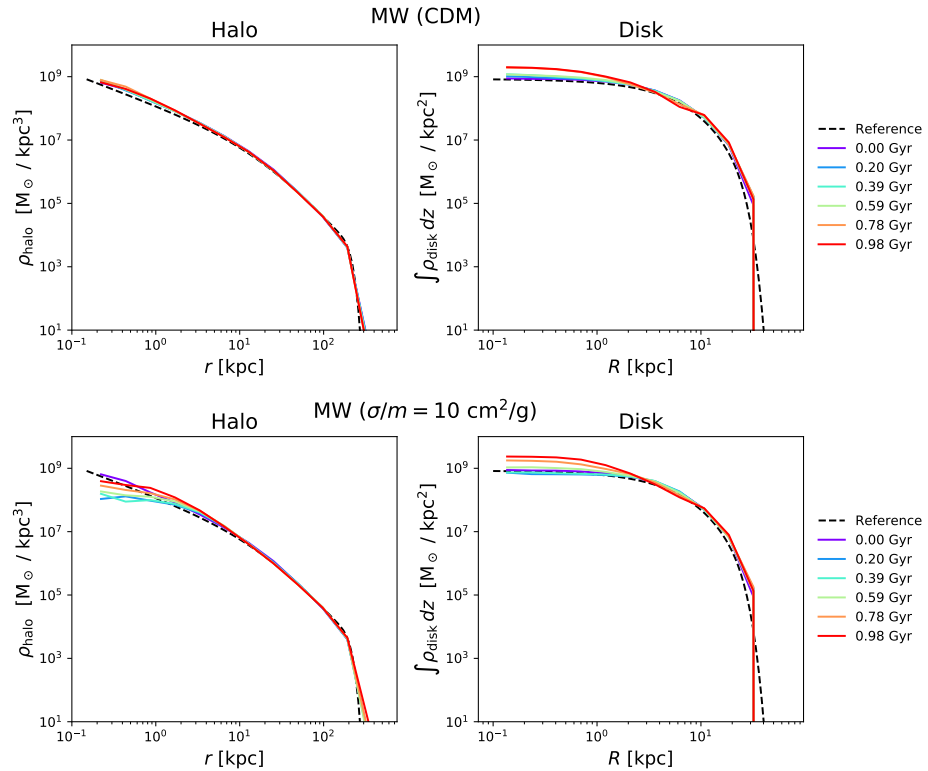


Figure 4.3: Evolution of the MW halo (left) and disk (right) during CDM (top) and SIDM ($\sigma/m = 10 \text{ cm}^2/\text{g}$) equilibration runs. The dashed line on the halo plots is the reference NFW distribution; on the disk plots it is the reference exponential-sech² distribution.

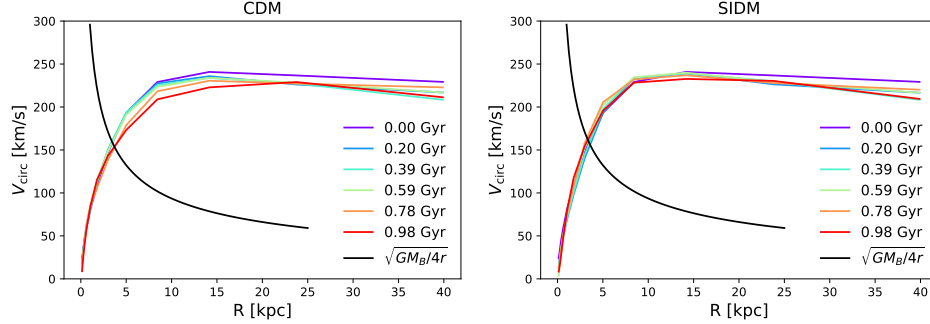


Figure 4.4: Evolution of rotation curves over time for the Milky Way disk in both the CDM and SIDM microphysics runs. Also plotted in black is $\sqrt{GM_B/4r}$, the circular velocity at the scale radius which would be expected if the disk mass followed a Hernquist profile.

where M_B is the mass of the baryons in the disk and V_B is the circular velocity of baryons at the given radius. Together, these imply that $V_B(r_0) = \sqrt{GM_B/4r_0}$. After truncation, our disk has a total mass of $M_B = 8.1 \times 10^{10} M_\odot$. Thus, we can plot the rotation curve of our disk and look for its intersection with $\sqrt{GM_B/4r_0}$. This should give us the values of r_0 and $V_B(r_0)$. The rotation curves for both the CDM and SIDM curves are plotted in Figure 4.4. They show $r_0 \approx 3.5$ kpc with a corresponding circular velocity $V_B(r_0) \approx 160$ km/s.

Looking back at Figure 4.3, we can estimate the central density of the halo to be $\rho_0 \approx 10^9 M_\odot/\text{kpc}^3$. We can also compute the central velocity dispersion by finding the root mean square of the radial velocities for the stars in the inner 5 kpc. For the late CDM snapshots, this measure gives $\sigma_0 = 123$ km/s. With all these quantities, we can compute $a_0 = 43.8$ and $a_1 = 6.6$. Plugging these in to Equation 2.33, we obtain an estimate for the core size of 0.37 kpc. This core size appears to be roughly consistent with the observed core size attained in the fully evolved SIDM distribution, though perhaps a little smaller.

For the Sgr equilibrations, however, we evolved the galaxy much farther for-

ward in time: approximately 10 Gyr for the CDM case and 20 Gyr for SIDM. These evolution times do not correspond to a physical orbit (especially given that the SIDM case would exceed the lifetime of the Universe). Rather, the initial Sgr disk distribution was found to be a bit unstable. We also wanted to be absolutely certain that the SIDM case would develop a cored profile. The evolution of the resulting Sgr mass profiles is shown in Figure 4.5.

In these plots, we see that the initial exponential-sech² distribution for the disk was not very close to equilibrium. Almost immediately, the disk redistributes itself more outwardly, with more of its mass at larger radii and a falling inner density. In the case of CDM physics, this happens within the first two Gyr, and the distribution holds relatively constant from there on. In the SIDM case, however, the distribution appears to continue to adjust, with the central density falling to around half that of the CDM disk.

In the case of the halo, we notice that the distribution holds relatively constant in the CDM case and agrees well with the reference NFW distribution. In the SIDM case, however, we see the slow development of a small core at low radii. This core appears to have a size of ≈ 1 kpc.

We can again apply the analytic expressions derived before to obtain an estimate for the expected core size. In this case, we note that the Sgr galaxy is well-approximated by the dark matter-dominated limit, so we will use the corresponding limit of the approximate core size. We again take $r_0 = 3.5$ kpc, and we estimate $\rho_0 \approx 10^{7.5} M_\odot/\text{kpc}^3$ from Figure 4.5. We again compute the central velocity dispersion by finding the root mean square of the radial velocities for the stars in the inner 5 kpc, which in this case is $\sigma_0 = 26$ km/s. Using Equation 2.32, we obtain an estimated core size of ≈ 1.3 kpc. We find this to roughly correspond to the core seen in the final time stamp of the evolved mass density profile.

With the equilibrated MW and Sgr galaxies in both the cuspy and cored régimes, we combine them to give us two initial conditions for mergers: cuspy

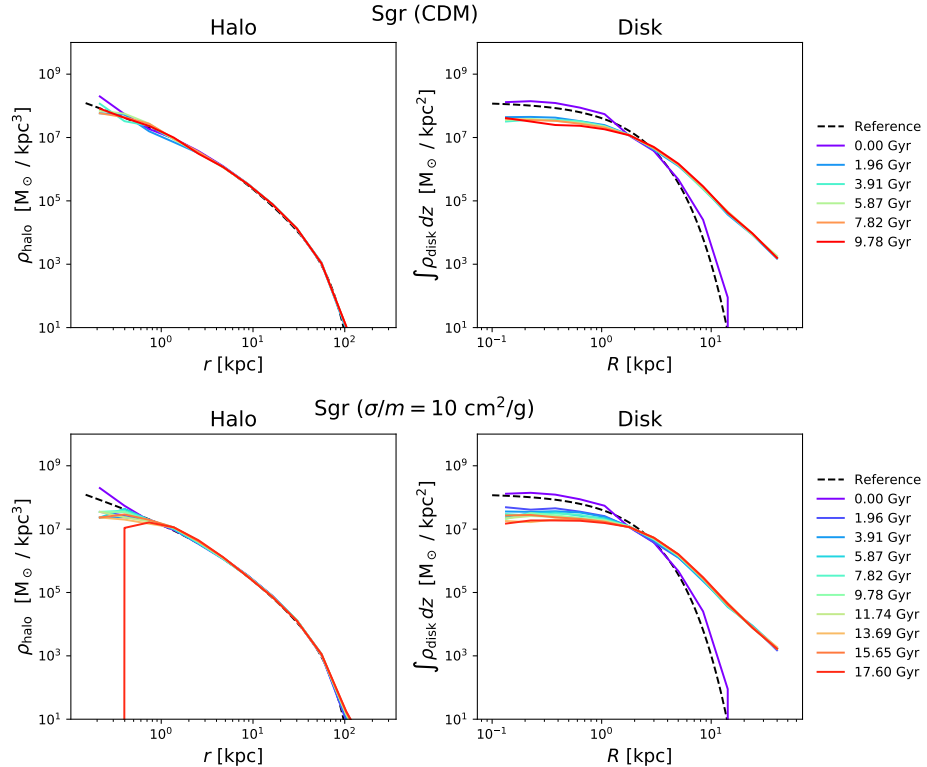


Figure 4.5: Evolution of the Sgr halo (left) and disk (right) during CDM (top) and SIDM (bottom) equilibration runs. The dashed line on the halo plots is the reference NFW distribution; on the disk plots it is the reference exponential-sech² distribution. We note in particular that the SIDM run results in generally depressed densities for both the halo and disk at low radii.

and cored. The Milky Way is left at its position from the equilibration run, as its center of mass will be close to the origin and its net velocity will be close to zero. Sgr is placed such that its center of mass lies at the point [125, 0, 0] and is given an initial velocity [−10, 0, 70]. These values correspond to the best fit values found in [59].

Chapter 5

Full infall simulations

5.1 Description and initial results

With the equilibrated and merged initial conditions for both cuspy (CDM) and cored (SIDM) galaxies, we now carry out our full simulations of the Sgr infall. We will consider *three* mergers: the cuspy initial conditions evolved using CDM microphysics, the cored initial conditions evolved with CDM microphysics, and the cored initial conditions evolved with SIDM microphysics. As before, we take $\sigma/m = 10 \text{ cm}^2/\text{g}$ in the SIDM case. These three mergers will be referred to as CDM/cusp, CDM/core, and SIDM respectively. By performing all three simulations, we will ideally be able to identify whether certain discrepancies between the CDM/cusp and the SIDM runs are the result of a cored initial profile or from the inclusion of self-interactions.

For each merger, the infall is simulated for 10 Gyr, with snapshots saved every 0.978 Gyr. In Figure 5.1, we show the positions of the both the stellar and dark matter particles of Sgr in the orbital plane at several times for each merger.

Even from these plots, there are some interesting patterns to note. First, we

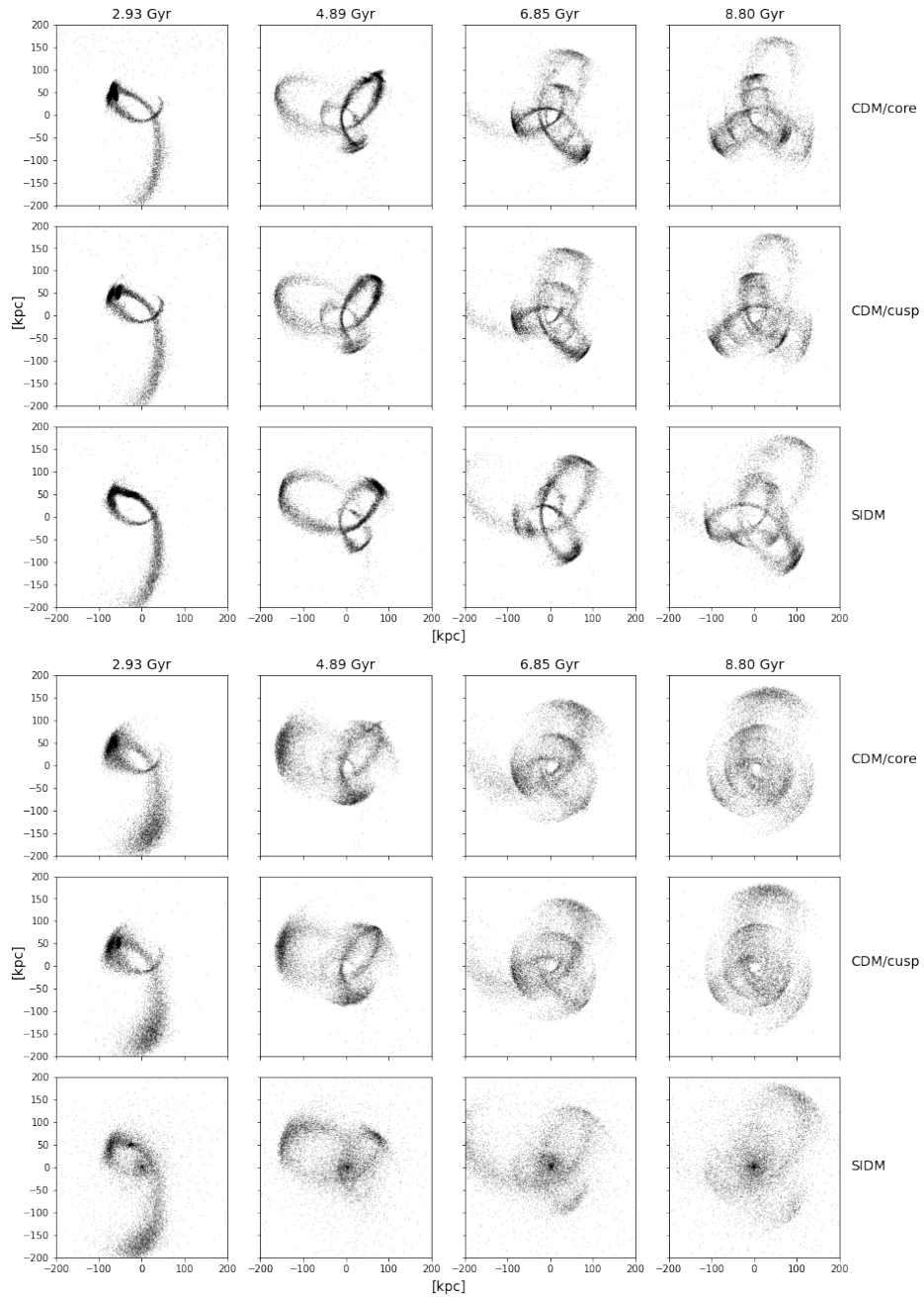


Figure 5.1: Positions of Sgr stellar (top three rows) and dark matter (bottom three rows) particles at various times for all three of the considered mergers. Each column denotes a different time; each row a different merger.

notice the development of a winding stream structure much like that reported in [59] by around 6 to 7 Gyr in all three cases. We can also note that the CDM/core and CDM/cusp are rather similar. There are some discernible differences, but the general shape and size of the stream structure is fairly similar throughout.

There are quite marked differences between the SIDM and CDM cases, however. The stream arms appear to be slightly rotated clockwise relative to the CDM mergers, and the general shape of the inner structure is very different. These differences are even more apparent when looking at the distribution of dark matter. In the CDM mergers, the dark matter distribution appears to roughly trace out the distribution of the stream and has a distinct hole at the origin. In the SIDM merger, however, the dark matter distribution largely loses the shape of the stream, instead collapsing inward toward the MW center.

We can also look at the density of particles in the orbital plane by performing a two-dimensional histogram on the data in Figure 5.1. The result is shown in Figure 5.2. The densities are integrated over the axis perpendicular to the orbital plane.

The density plots allow us to more strictly quantify some of the trends noted previously. For example, the dark matter density plots show quite concretely that the dark matter distribution in the SIDM case peaks at the Galactic center, where there is a distinct hole in the CDM mergers. The SIDM particles are also significantly less well-constrained, with a large spread extending beyond the limits of the plot. This is compared to the CDM cases, where there are relatively few particles outside of the path of the stream.

Looking at the density distribution of the stellar particles allows us to quantify some of the differences noted earlier. For example, at 6.85 Gyr, the SIDM stream has a relatively high-density ($\sim 10^5 M_\odot/\text{kpc}^2$) stream arc extending from approximately $(-20, 0)$ up to around $(60, 125)$. The corresponding arc

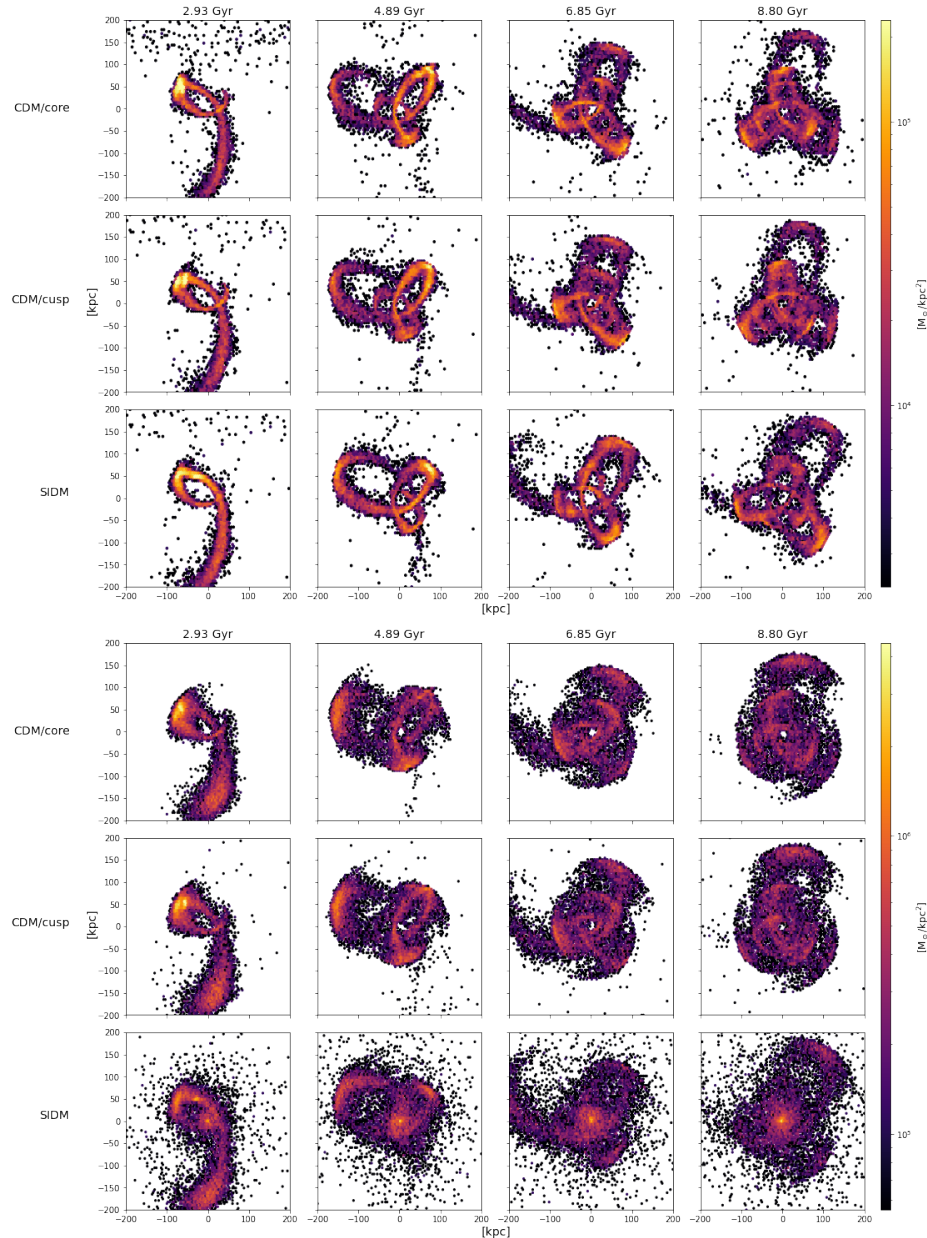


Figure 5.2: Two-dimensional density histogram of the stellar (top three rows) and dark matter (bottom three rows) Sgr particles at various times for each considered merger. Densities are integrated over the axis perpendicular to the orbital plane.

exists in the CDM cases, but it is less well-defined (there is more horizontal spread) and lower density ($\sim 10^4 M_\odot/\text{kpc}^2$).

There are other, similar differences, but we would do better to analyze these differences for the specific time stamps of each merger which most closely approximate Sgr today. Determining this requires mapping the position of the Sgr progenitor, however.

5.2 Identifying the Sgr progenitor

A key part of analyzing these data is to understand the trajectory and evolution of the Sgr progenitor. As such, we desire a method for successfully identifying the position of the Sgr progenitor throughout its evolution. This is less straightforward than it may sound because of the strong effects of tidal stripping. These mean that we need to identify which particles are stripped or bound to the progenitor at any given point and omit stripped particles from our calculation of the progenitor position. In our tests, we tried a few different methods which we will describe here.

The first method that we tried was to track bound versus unbound star particles by counting particles as stripped once they exceeded a fixed radius from the center of mass of bound particles. The algorithm for this is as follows. We begin by counting the stellar particles within a certain radius on the first snapshot to be “bound”. For each snapshot after, we find the center of mass of the bound particles. Then, for each bound particle, we compute its distance from the center of mass. If this exceeds the fixed stripping radius, we unmark the star as bound and continue.

As stated, this algorithm leaves has two parameters that can be tuned: the initial stripping radius for the initial Sgr stellar positions and the fixed stripping radius for all following snapshots. We found it useful to describe the initial stripping radius instead in terms of the percentage of particles that are

initial counted as “bound”. For example, we say that the we start with the innermost 20% of particles and proceed with a fixed radius of 20 kpc. effective for our mergers. The results of applying this algorithm to the CDM/Cusp merger data with a few different choices of parameters can be seen in Figure 5.3.

This figure shows us that starting with too few of the initial particles (in this case, 20%) leads to very small numbers of bound particles at late times. Further, it shows us that the trajectory of the progenitor can be somewhat sensitive to the chosen algorithm parameters, especially at late times.

This algorithm appears to have two issues that we want to try to solve. First, the actual size of the progenitor is expected to shrink with time, as progressively more of the particles are stripped. By using a fixed stripping radius, we are not modeling the expected decay of the progenitor size. The second problem we encountered is that this method appears to leave us with only $\mathcal{O}(10)$ bound particles after around 6 Gyr evolved. As such, we decided to explore modifications to the algorithm.

The first modification was to consider a decreasing stripping radius. The algorithm is very similar to before. On the first snapshot, we count some inner fraction of the particles to be “bound” and find the radius of this ball of bound particles. For the next snapshot, we strip any particles which exceed this radius (times a constant). *However*, after stripping away particles, we recompute the radius of the ball of the bound particles, and reset the stripping radius equal to this. For each snapshot following, we strip particles that are beyond this radius and recompute the radius. Over time, the stripping radius will decrease, modeling the progressively decreasing size of the progenitor. However, these modifications tend to make the algorithm a bit *too* aggressive, with it stripping away all the particles in some cases. We introduced a minimum stripping radius such that the algorithm would choose the maximum of the given minimum and the computed radius, but we found

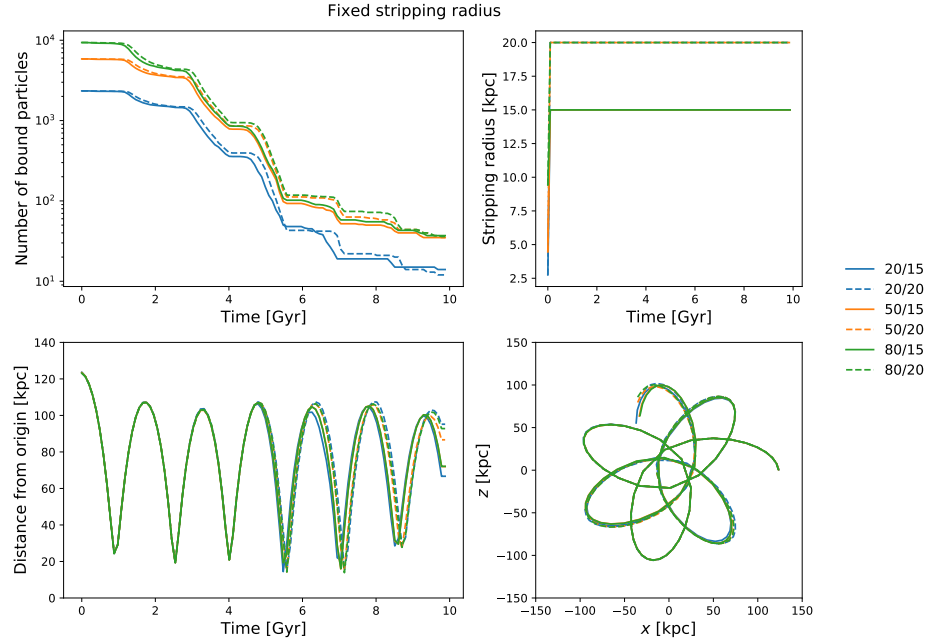


Figure 5.3: Results of applying the “fixed stripping radius” progenitor-identifying algorithm to the CDM/cusp merger data. Entries in the legend are given in the following format: “a/b” means that we started with the innermost “a”% of stellar particles and proceeded with a fixed stripping radius of “b” kpc. In the upper left is the number of bound particles over time. The upper right shows the stripping radius. The bottom left shows the distance from the origin to the Sgr center of mass; an estimate of the MW-Sgr separation. The bottom right shows the trajectory of the progenitor in the orbital plane.

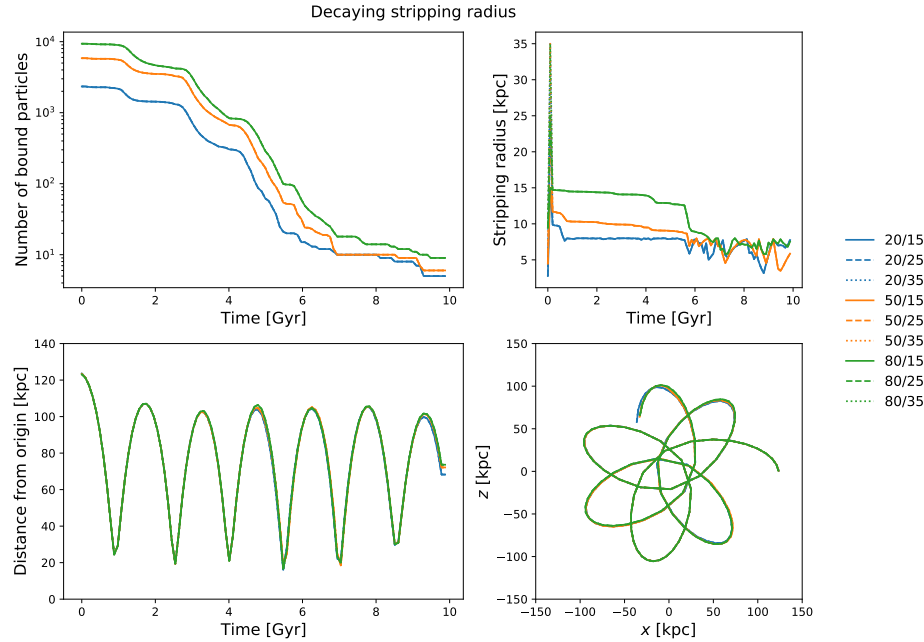


Figure 5.4: Results of applying the “decaying stripping radius” progenitor-identifying algorithm to the CDM/cusp merger data with a minimum stripping radius of 8 kpc. Plots have same meaning as in Figure 5.3.

that the behavior in this case reduced to that of the fixed-radius algorithm. The results of this decaying stripping radius are shown in Figure 5.4, with a minimum allowed stripping radius of 8 kpc.

As can be seen in the figure, this algorithm leads to very aggressive stripping. No matter the initial conditions, the desired stripping radius falls *very* quickly. For all considered parameter combinations, the desired stripping radius fell below 8 kpc before the 6 Gyr mark, at which point the algorithm will just default to using a fixed 8 kpc stripping radius. This indicates that these changes are simply too aggressive and, when bundled with a minimum stripping radius, is effectively equivalent to the fixed stripping radius scheme.

One possible reason that it becomes too aggressive is because the actual size

of the progenitor is not monotonically decreasing. Rather, its size fluctuates over the course of the orbit, becoming quite compressed and small near the pericenter and a bit more spread out and large near the apocenter. These effects are modeled by the King formula for the tidal radius (todo cite King) as given in [59]:

$$r_t = r \left[\frac{1}{2} \frac{M_{\text{Sgr}}(<r_t)}{M_{\text{MW}}(<r)} \right]^{1/3}, \quad (5.1)$$

where $M_{\text{gal}}(<r)$ is the enclosed halo mass in galaxy “gal” within radius r of the center of mass of the galaxy, r is the distance between the Milky Way and Sgr centers of mass, and r_t is the tidal radius. For a given snapshot, then, we can compute the tidal radius according to this formula by subtracting r_t from both sides and using a simple root finder to identify the r_t which solves the equation. We then strip any particles which are farther than r_t away from the center of mass of the progenitor at the current time. The results of using the King tidal radius are shown in Figure 5.5. Again, we pair this algorithm with a minimum stripping radius of 8 kpc.

Yet again, this algorithm appears to simply be too aggressive. In all cases, the tidal radius quickly dips below the minimum stripping radius of 8 kpc. Further, the algorithm appears to be somewhat unstable, defaulting to a recommended radius of just *zero* beyond a certain threshold. When this occurs, the algorithm defaults to a fixed stripping radius equal to the minimum. Again, then, this algorithm offers no improvements over the fixed radius.

At this point, it seems like the issue of too few bound particles at late times may be a problem related to our relatively small number of Sgr stellar particles instead of a problem with the algorithms themselves. As such, we decided to try to use the fixed algorithm but using both stellar *and* dark matter particles. The result on the CDM/cusp data is shown in Figure 5.6.

This appears to yield promising results. We note that there are generally

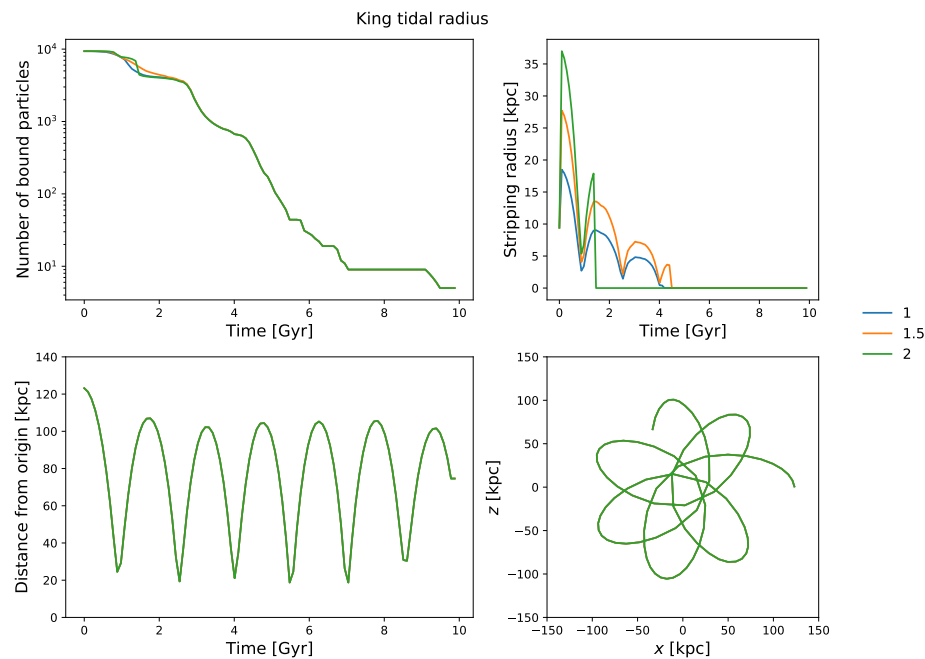


Figure 5.5: Results of using the “King tidal radius” progenitor-identifying algorithm on the CDM/cusp merger data with a minimum stripping radius of 8 kpc. The legend entries correspond to a fixed constant multiplied against the tidal radius before performing stripping. Plots again have the same meaning as in Figure 5.3.

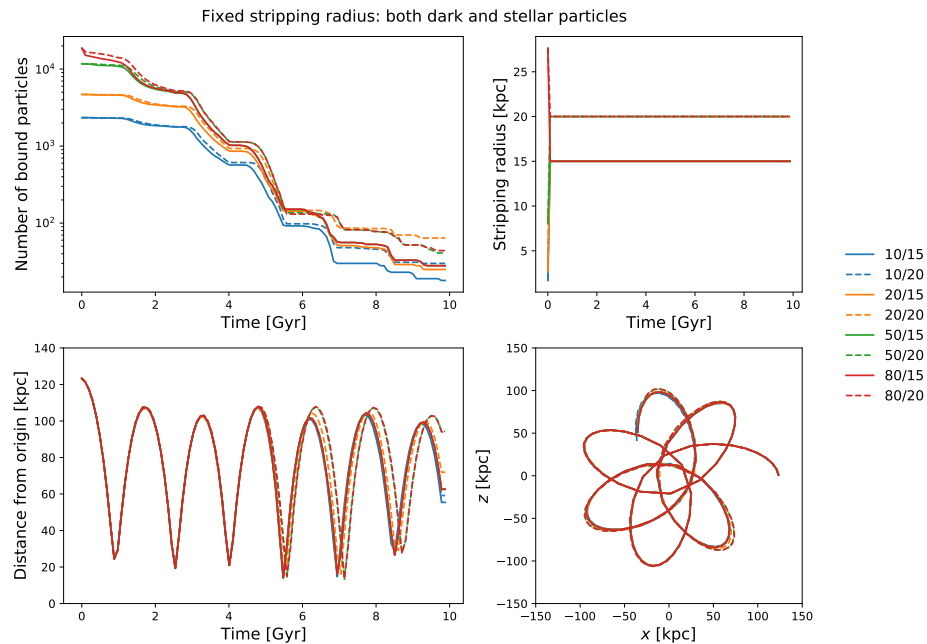


Figure 5.6: Results of using the “fixed stripping radius” progenitor-identifying algorithm on the all particles in the CDM/cusp merger data. Plots and legend entries have the same meaning as in Figure 5.3.

more “bound” particles at late times when using all particles than when only using stellar ones, and that, aside from the “50/20” and “80/20” runs, the resulting trajectories appear to be more robust to the algorithm parameters. As such, we choose to move forward with this algorithm using the “20/20” parameters, as they appear to be consistent with the majority of the other parameter choices and yield the most bound particles in the end. Using these choices to identify the progenitor, we apply the algorithm to all three mergers. The resulting data are shown in Figure 5.7.

The plots in this figure are evidence that SIDM microphysics may indeed have a profound impact on the resulting trajectory of the Sgr satellite. One difference can be seen in that the number of bound particles decreases much more substantially at early times than either of the two CDM runs. This could be explained by considering that self-interactions provide a mechanism for dark matter to free itself from shallow gravitational potential wells to which collisionless dark matter would remain confined.

Looking at the MW-Sgr separation over time, it is immediately evident that the cored profile yields a slightly longer orbital period, given the slowly increasing distance between the apo- and pericenters of the CDM/cusp and CDM/core orbits. The inclusion of self-interactions appears to add to this effect, with the CDM/cusp attaining six pericenters before the SIDM orbit is able to reach a fifth.

One phenomenon showcased by the separation curves which is difficult to understand is the lack of a consistent decay in the apocenters. We compare to figure 6 of [59], which shows a steadily decreasing pericenter. This is the expected behavior; as the Sgr progenitor orbits and decays, we would expect it to lose energy and steadily fall inward. This, however, does not appear in our plots. In fact, this phenomenon is exacerbated in the SIDM merger, where the apocenter actually appears to *grow* after around 4 Gyr, reaching nearly 130 kpc at the 6 Gyr mark. The mechanism by which this would

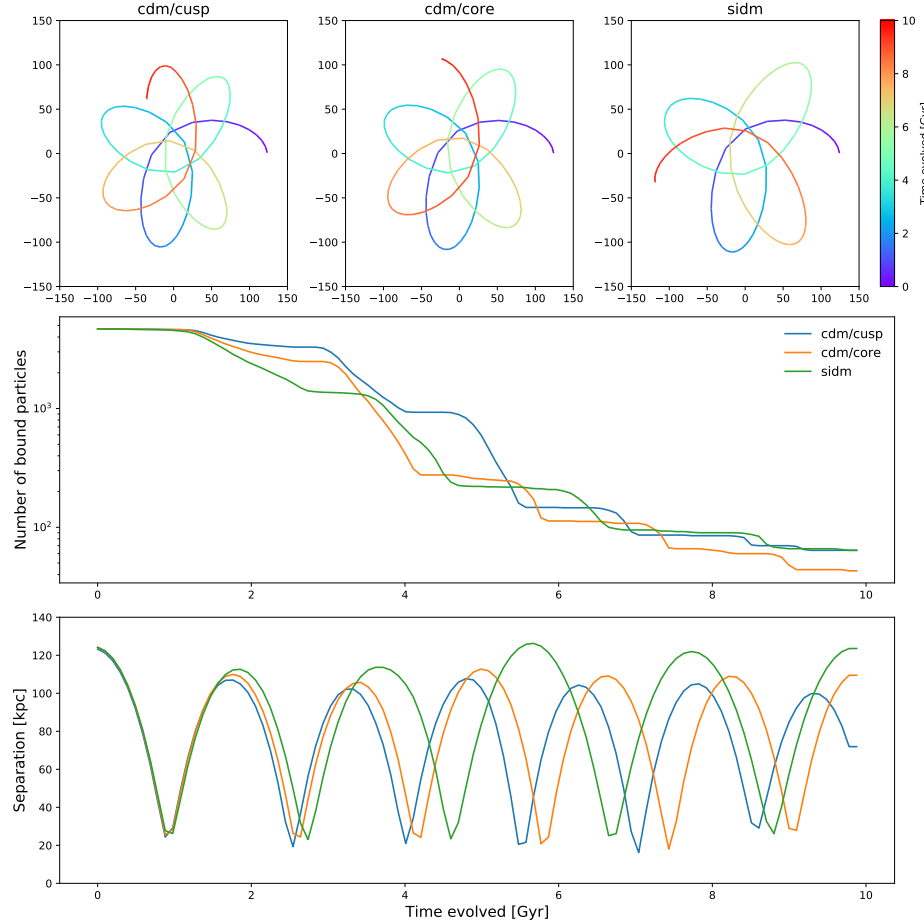


Figure 5.7: Results of using the “fixed stripping radius” progenitor-identifying algorithm on all the particles in each of the mergers. We use the “20/20” algorithm parameters for all mergers, meaning that we start with the inner 20% of particles and use a 20 kpc stripping radius. The top row shows the trajectory of the Sgr progenitor in the orbital plane for each merger. The middle row plot shows the number of bound particles over time. The bottom row plot shows the MW-Sgr separation over time.

occur is not yet understood.

5.3 Time of closest match

As stated previously, a description of the orbit of the progenitor will allow us to determine the specific time stamps at which our mergers most closely approximate Sgr today. We take the observed coordinates of Sgr to be $(\alpha, \delta) = (283.83, -29.45)$ (where α is right ascension and δ is declination) degrees [65], proper motion $(\mu_\alpha \cos \delta, \mu_\delta) = (-2.54 \pm 0.18, -1.19 \pm 0.16)$ mas/yr [66], distance 24.8 ± 0.8 kpc [57], and line-of-sight velocity 179 ± 1 km/s [59, 67]. We can then convert the coordinates of the Sgr progenitor to equatorial coordinates and look at the evolution over time, comparing against these reference values. The result is shown in Figure 5.8.

We can also focus specifically on the position of the progenitor instead of its velocity, looking specifically at the right ascension, declination, and distance. We find the orbit to be strongly period in right ascension, so these plots have been “unwrapped” to better show the evolution of the progenitor over time. The results are shown in Figure 5.9.

We note that the Dierickx 2017 model [59] most closely approximated the observed coordinates just after its fifth pericenter. We note that no snapshot of our model comes as close to these coordinates as theirs, but we believe that this discrepancy would be alleviated somewhat by greater time resolution in the snapshots of the stream.

5.4 Comparison to stream data

The last piece of the analysis that we will consider is a comparison to observed data. The data we will compare against comes from the second data release (DR2) of the *Gaia* mission [68, 69], from which Sgr stars have been

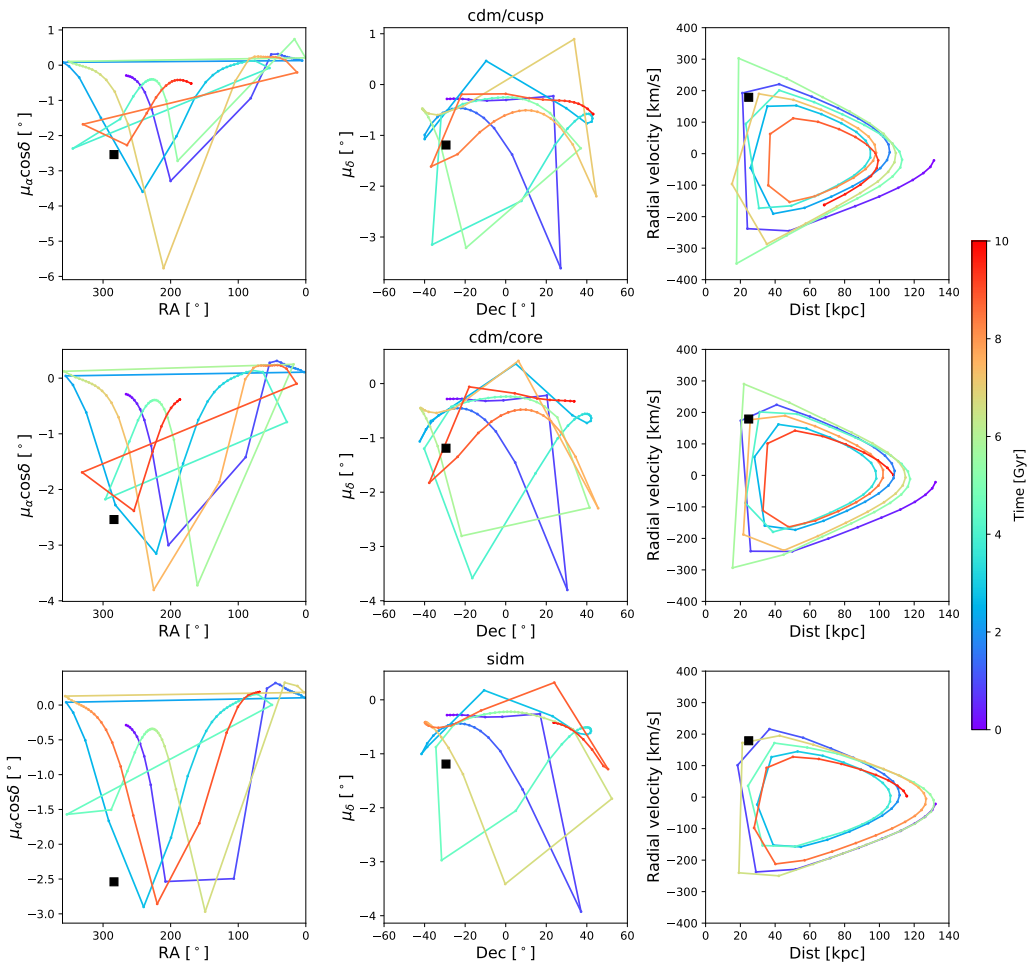


Figure 5.8: Trajectory of the Sgr progenitor in terms of equatorial coordinates and proper motions for each merger. Black squares represent the observed coordinates of the progenitor today.

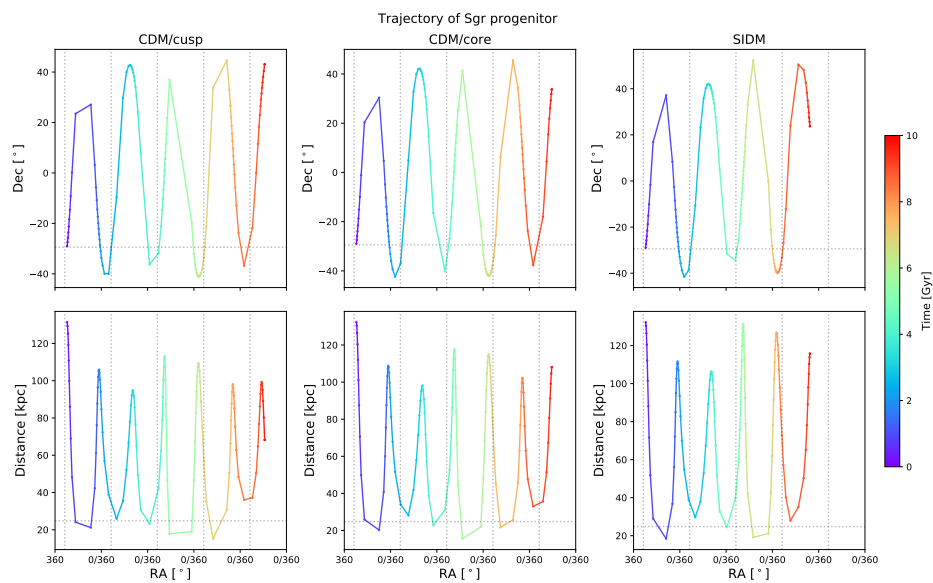


Figure 5.9: Trajectory of the simulated Sgr progenitor in terms of positional coordinates only. The orbit is periodic in right ascension, so the coordinates have been “unwrapped” to better show the behavior. Observed values of the right ascension, declination, and distance are shown as dashed lines.

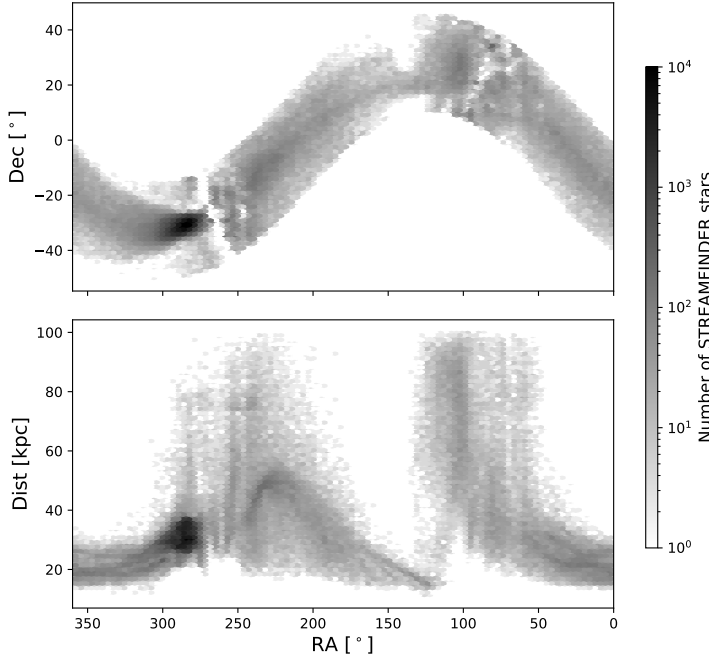


Figure 5.10: Equatorial coordinates and estimated distances for the 263,438 Sgr stars identified by the **STREAMFINDER** algorithm.

identified by Ibata et al. [70] using the **STREAMFINDER** algorithm [71, 72]. The resulting dataset includes the *Gaia* equatorial coordinates, proper motions, magnitudes, and colors of 263,438 stars, along with an estimate of the distance provided by the algorithm. They find their dataset to agree well with the Law and Majewski 2010 model [58], barring a few small deviations. The **STREAMFINDER** sample is shown in Figure 5.10.

In the Dierickx 2017 model [59], the simulation was found to most closely approximate the position of Sgr today at the fifth pericenter. As such, we consider the corresponding times in our mergers. In our mergers, we find the fifth pericenter to occur after 7.0 Gyr in the CDM/cusp merger, 7.4 Gyr in the CDM/core merger, and 8.8 Gyr in the SIDM merger.

For each merger at the corresponding times, we convert the coordinates of

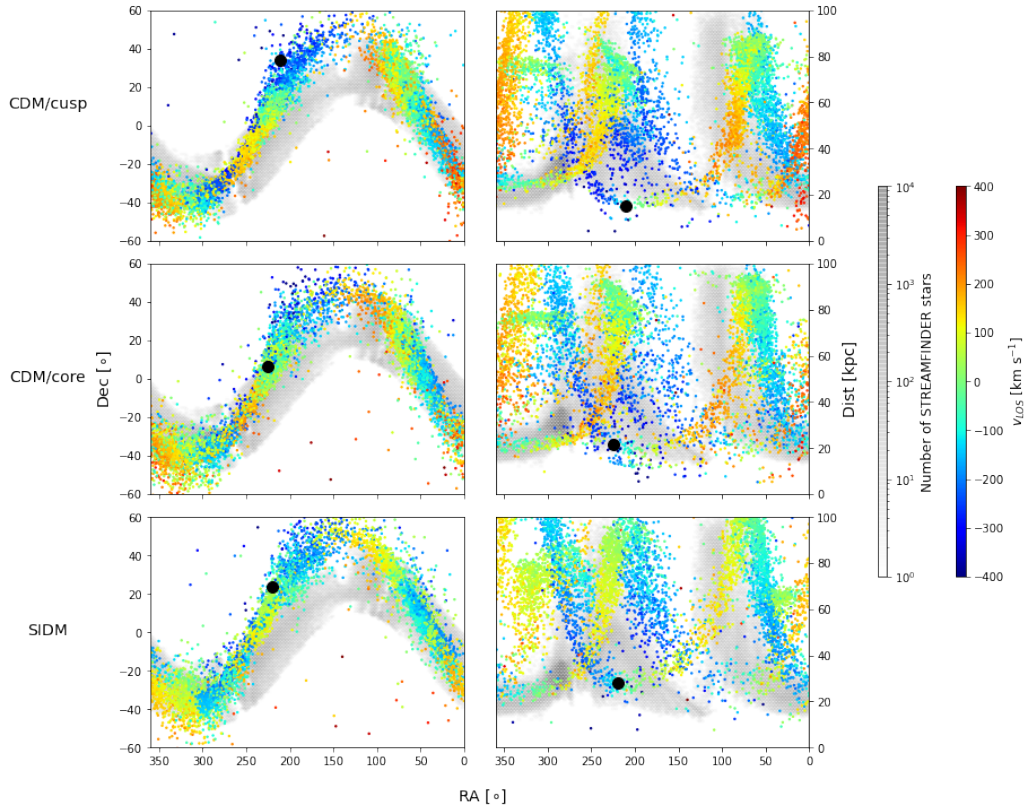


Figure 5.11: Equatorial coordinates for our simulated Sgr stellar particles of distances less than 100 kpc at the time of the fifth pericenter for each merger. The position of the progenitor is shown by a black circle. The density of STREAMFINDER stars is also shown in gray.

the stellar particles into equatorial coordinates in the ICRS frame using the Astropy package [73, 74]. We only consider stars with distances less than 100 kpc, as this is done in [59] and the STREAMFINDER sample contains no stars beyond this threshold. The resulting coordinates are plotted in Figure 5.11, with the STREAMFINDER density plot shown in gray.

Our comparison to the STREAMFINDER stars shows qualitatively good agreement in terms of the right ascension and declination. The thickness of the stream appears to be narrower in some places, and our maximum achieved

declination is approximately 60° where the **STREAMFINDER** data barely exceeds 40° . We also see qualitative agreement for the primary stream arms in terms of distance, though our stream appears to be shifted relative to the **STREAMFINDER** data. Our model also predicts an extension to the Sgr stream arms, similar to the results of Dierickx et al. [59].

There also exist some differences between the three mergers in this frame. For example, the CDM/cusp run appears to have more particles with larger line-of-sight velocity magnitudes, with more stars that appear to be dark blue and red. Inversely, the SIDM merger appears to have much more limited variation in line-of-sight velocity. Also, the SIDM and CDM runs appear to have different features which are well-defined; the CDM runs show a rising stream arm at right ascension $\approx 350^\circ$ that is not well-represented in the SIDM run. The SIDM run, however, has a more well-defined falling stream arm at right ascension $\approx 200^\circ$.

To more fully explore these distances, we can look at histograms of the stellar particles' equatorial coordinates and proper motions and compare to the same for the **STREAMFINDER** stars. We note, however, the presence of a very dense region of stars in the **STREAMFINDER** data at RA = 290° , Dec = -30° , and dist = 30 kpc. This greatly skews the **STREAMFINDER** distributions, so we cut it off in the plots in order to more fully elucidate the simulation distributions. The resulting histograms may be seen in Figure 5.12.

The histograms show us that the distributions of simulated stars are quite different than the **STREAMFINDER** sample, particularly when we consider the proper motions and distances. Specifically, the $\mu_\alpha \cos \delta$ distribution is largely concentrated between -1 and 0.5 mas/yr for all three mergers, but appears to be a roughly unimodal distribution at -2.5 mas/yr in the **STREAMFINDER** data. Similarly, all three mergers show a strong peak in μ_δ at approximately -0.5 mas/yr, compared to the strong peak at -1.5 mas/yr in the **STREAMFINDER** set. In the distance distribution, we see the distribution of

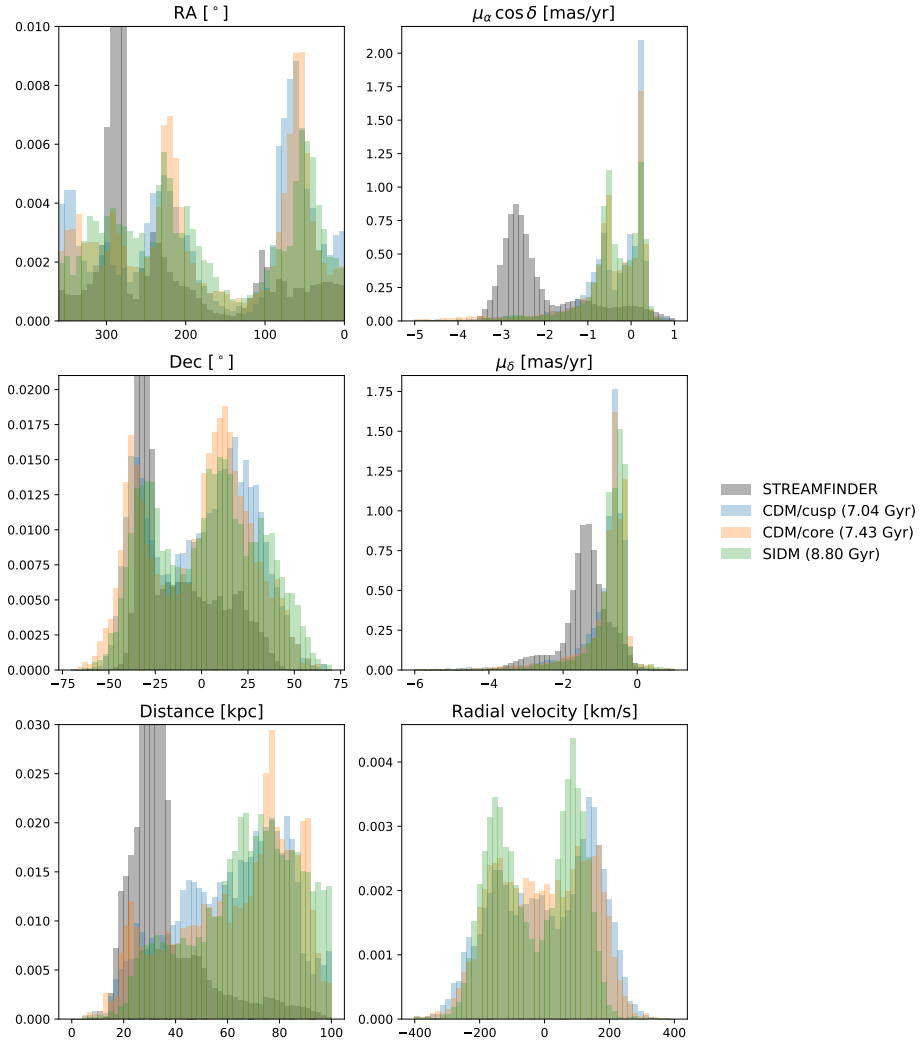


Figure 5.12: Histograms of the equatorial coordinates and proper motions of the simulated stellar particles closer than 100 kpc and the reference STREAMFINDER stars (where possible). Note that the STREAMFINDER sample contains a very dense region which is intentionally cut off in the right ascension, declination, and distance plots in order to better see the simulated distributions. All distributions are normalized to unity.

distances appear to rise until around 60 to 80 kpc, compared to the sharp peak around 30 kpc in the **STREAMFINDER** set with a decreasing frequency for larger distances.

The declination plot shows the existence of peaks around -30° to -40° for all mergers and the **STREAMFINDER** set. However, the mergers *also* have a peak at around $+20^\circ$ that appears to be largely non-existent in **STREAMFINDER**. Lastly, we note that the right ascension plot shows some similarities between all mergers and the **STREAMFINDER**: particularly, a peak at around 225° and a trough at around 140° .

The histograms also allow us to highlight some differences between the mergers themselves. In particular, the radial velocity histogram confirms the previously noted trend. The CDM/cusp merger appears to have more particles with higher radial velocity magnitudes than either of the other runs. The CDM/core merger appears to have a much flatter distribution of radial velocities than either of the other two mergers. The SIDM merger, on the other hand, has a strongly bimodal distribution of radial velocities, with strong peaks around $+100$ and -150 km/s.

Bibliography

- [1] J. H. Oort. “The force exerted by the stellar system in the direction perpendicular to the galactic plane and some related problems”. In: *Bulletin of the Astronomical Institutes of the Netherlands* 6 (Aug. 1932), p. 249. ISSN: 0365-8910. URL: <http://adsabs.harvard.edu/abs/1932BAN.....6..2490> (visited on 04/19/2021).
- [2] Virginia Trimble. “Existence and Nature of Dark Matter in the Universe”. en. In: *Annu. Rev. Astron. Astrophys.* 25.1 (Sept. 1987), pp. 425–472. ISSN: 0066-4146, 1545-4282. DOI: 10.1146/annurev.aa.25.090187.002233. URL: <http://www.annualreviews.org/doi/10.1146/annurev.aa.25.090187.002233> (visited on 03/22/2021).
- [3] F. Zwicky. “Die Rotverschiebung von extragalaktischen Nebeln”. In: *Helvetica Physica Acta* 6 (1933), pp. 110–127. ISSN: 0018-0238. URL: <http://adsabs.harvard.edu/abs/1933HPh.....6..110Z> (visited on 04/19/2021).
- [4] Heinz Andernach and Fritz Zwicky. “English and Spanish Translation of Zwicky’s (1933) The Redshift of Extragalactic Nebulae”. In: *arXiv:1711.01693 [astro-ph]* (Nov. 2017). arXiv: 1711.01693. URL: <http://arxiv.org/abs/1711.01693> (visited on 04/19/2021).
- [5] Horace W. Babcock. “The rotation of the Andromeda Nebula”. In: *Lick Observatory Bulletin* 19 (1939), pp. 41–51. ISSN: 0075-9317. DOI: 10.

- 5479/ADS/bib/1939LicOB.19.41B. URL: <http://adsabs.harvard.edu/abs/1939LicOB..19...41B> (visited on 04/19/2021).
- [6] J. H. Oort. “Some Problems Concerning the Structure and Dynamics of the Galactic System and the Elliptical Nebulae NGC 3115 and 4494.” en. In: *ApJ* 91 (Apr. 1940), p. 273. ISSN: 0004-637X, 1538-4357. DOI: 10.1086/144167. URL: <http://adsabs.harvard.edu/doi/10.1086/144167> (visited on 04/19/2021).
- [7] W. Lohmann. “Die Masse der Galaxis”. de. In: *Z. Physik* 144.1-3 (Feb. 1956), pp. 66–75. ISSN: 1434-6001, 1434-601X. DOI: 10.1007/BF01327068. URL: <http://link.springer.com/10.1007/BF01327068> (visited on 04/19/2021).
- [8] Thornton Page. “Average Masses and Mass-Luminosity Ratios of the Double Galaxies.” In: *The Astrophysical Journal* 132 (Nov. 1960), pp. 910–912. ISSN: 0004-637X. DOI: 10.1086/146995. URL: <http://adsabs.harvard.edu/abs/1960ApJ...132..910P> (visited on 04/19/2021).
- [9] Erik Holmberg. “On the masses of double galaxies”. In: *Meddelanden fran Lunds Astronomiska Observatorium Serie I* 186 (June 1954), pp. 1–20. URL: <http://adsabs.harvard.edu/abs/1954MeLuF.186....1H> (visited on 04/19/2021).
- [10] Virginia Trimble. “History of Dark Matter in Galaxies”. In: *Planets, Stars, and Stellar Systems: Galactic Structure and Stellar Populations*. Ed. by Terry D. Oswalt and Gerard Gilmore. Vol. 5. Dordrecht: Springer Netherlands, 2013, pp. 1091–1118.
- [11] Vera C. Rubin and W. Kent Ford Jr. “Rotation of the Andromeda Nebula from a Spectroscopic Survey of Emission Regions”. In: *The Astrophysical Journal* 159 (Feb. 1970), p. 379. ISSN: 0004-637X. DOI: 10.1086/150317. URL: <http://adsabs.harvard.edu/abs/1970ApJ...159..379R> (visited on 04/19/2021).
- [12] M. S. Roberts and A. H. Rots. “Comparison of Rotation Curves of Different Galaxy Types”. In: *Astronomy and Astrophysics* 26 (Aug.

- 1973), pp. 483–485. ISSN: 0004-6361. URL: <http://adsabs.harvard.edu/abs/1973A%26A...26..483R> (visited on 04/19/2021).
- [13] M. S. Roberts and R. N. Whitehurst. “The rotation curve and geometry of M31 at large galactocentric distances.” In: *The Astrophysical Journal* 201 (Oct. 1975), pp. 327–346. ISSN: 0004-637X. DOI: 10.1086/153889. URL: <http://adsabs.harvard.edu/abs/1975ApJ...201..327R> (visited on 04/19/2021).
- [14] Jaan Einasto et al. “Missing mass around galaxies: morphological evidence”. en. In: *Nature* 252.5479 (Nov. 1974). Number: 5479 Publisher: Nature Publishing Group, pp. 111–113. ISSN: 1476-4687. DOI: 10.1038/252111a0. URL: <https://www.nature.com/articles/252111a0> (visited on 04/19/2021).
- [15] J. P. Ostriker, P. J. E. Peebles, and A. Yahil. “The size and mass of galaxies, and the mass of the universe”. In: *The Astrophysical Journal Letters* 193 (Oct. 1974), pp. L1–L4. ISSN: 0004-637X. DOI: 10.1086/181617. URL: <http://adsabs.harvard.edu/abs/1974ApJ...193L..10> (visited on 04/19/2021).
- [16] J. P. Ostriker and P. J. E. Peebles. “A Numerical Study of the Stability of Flattened Galaxies: or, can Cold Galaxies Survive?” In: *The Astrophysical Journal* 186 (Dec. 1973), pp. 467–480. ISSN: 0004-637X. DOI: 10.1086/152513. URL: <http://adsabs.harvard.edu/abs/1973ApJ...186..467O> (visited on 04/19/2021).
- [17] Peter Schneider. *Extragalactic Astronomy and Cosmology*. en. Berlin, Heidelberg: Springer Berlin Heidelberg, 2015. ISBN: 978-3-642-54082-0 978-3-642-54083-7. DOI: 10.1007/978-3-642-54083-7. URL: <http://link.springer.com/10.1007/978-3-642-54083-7> (visited on 03/22/2021).
- [18] Adam G. Riess et al. “Observational Evidence from Supernovae for an Accelerating Universe and a Cosmological Constant”. In: *The Astronomical Journal* 116 (Sept. 1998), pp. 1009–1038. ISSN: 0004-6256.

- DOI: 10.1086/300499. URL: <http://adsabs.harvard.edu/abs/1998AJ....116.1009R> (visited on 04/22/2021).
- [19] S. Perlmutter et al. “Measurements of Ω and Λ from 42 High-Redshift Supernovae”. In: *The Astrophysical Journal* 517 (June 1999), pp. 565–586. ISSN: 0004-637X. DOI: 10.1086/307221. URL: <http://adsabs.harvard.edu/abs/1999ApJ...517..565P> (visited on 04/22/2021).
- [20] Scott Dodelson and Fabian Schmidt. *Modern Cosmology*. en. 2nd ed. Elsevier, 2021. ISBN: 978-0-12-815948-4. DOI: 10.1016/B978-0-12-815948-4.00002-4. URL: <https://linkinghub.elsevier.com/retrieve/pii/B9780128159484000024> (visited on 03/23/2021).
- [21] Subhendra Mohanty. *Astroparticle Physics and Cosmology: Perspectives in the Multimessenger Era*. en. Vol. 975. Lecture Notes in Physics. Cham: Springer International Publishing, 2020. ISBN: 978-3-030-56200-7 978-3-030-56201-4. DOI: 10.1007/978-3-030-56201-4. URL: <http://link.springer.com/10.1007/978-3-030-56201-4> (visited on 03/22/2021).
- [22] Lars Bergström and Ariel Goobar. *Cosmology and particle astrophysics*. en. 2. ed., reprinted. Springer Praxis books in astronomy and planetary science. OCLC: 254584818. Berlin: Springer, 2008. ISBN: 978-3-540-32924-4.
- [23] James S. Bullock and Michael Boylan-Kolchin. “Small-Scale Challenges to the Λ CDM Paradigm”. In: *Annual Review of Astronomy and Astrophysics* 55 (Aug. 2017), pp. 343–387. ISSN: 0066-4146. DOI: 10.1146/annurev-astro-091916-055313. URL: <http://adsabs.harvard.edu/abs/2017ARA%26A..55..343B> (visited on 04/22/2021).
- [24] Carlos S. Frenk et al. “The formation of dark halos in a universe dominated by cold dark matter”. In: *The Astrophysical Journal* 327 (Apr. 1988), pp. 507–525. ISSN: 0004-637X. DOI: 10.1086/166213. URL: <http://adsabs.harvard.edu/abs/1988ApJ...327..507F> (visited on 04/19/2021).

- [25] John Dubinski and R. G. Carlberg. “The structure of cold dark matter halos”. In: *The Astrophysical Journal* 378 (Sept. 1991), pp. 496–503. ISSN: 0004-637X. DOI: 10.1086/170451. URL: <http://adsabs.harvard.edu/abs/1991ApJ...378..496D> (visited on 04/19/2021).
- [26] Julio F. Navarro, Carlos S. Frenk, and Simon D. M. White. “The Structure of Cold Dark Matter Halos”. In: *arXiv:astro-ph/9508025* (Aug. 1995). arXiv: astro-ph/9508025. DOI: 10.1086/177173. URL: <http://arxiv.org/abs/astro-ph/9508025> (visited on 04/19/2021).
- [27] James Binney and Scott Tremaine. *Galactic dynamics*. 2nd ed. Princeton series in astrophysics. Princeton: Princeton University Press, 2008. ISBN: 978-0-691-13026-2 978-0-691-13027-9.
- [28] Lars Hernquist. “An analytical model for spherical galaxies and bulges”. In: *The Astrophysical Journal* 356 (June 1990), pp. 359–364. ISSN: 0004-637X. DOI: 10.1086/168845. URL: <http://adsabs.harvard.edu/abs/1990ApJ...356..359H> (visited on 04/19/2021).
- [29] Julio F. Navarro, Carlos S. Frenk, and Simon D. M. White. “A Universal Density Profile from Hierarchical Clustering”. In: *arXiv:astro-ph/9611107* (Oct. 1997). arXiv: astro-ph/9611107. DOI: 10.1086/304888. URL: <http://arxiv.org/abs/astro-ph/9611107> (visited on 04/19/2021).
- [30] Ricardo Flores et al. “Rotation curves from baryonic infall - Dependence on disk-to-halo ratio, initial angular momentum, and core radius, and comparison with data”. In: *The Astrophysical Journal* 412 (Aug. 1993), pp. 443–454. ISSN: 0004-637X. DOI: 10.1086/172934. URL: <http://adsabs.harvard.edu/abs/1993ApJ...412..443F> (visited on 04/19/2021).
- [31] Joshua D. Simon. “The Faintest Dwarf Galaxies”. In: *Annual Review of Astronomy and Astrophysics* 57 (Aug. 2019), pp. 375–415. ISSN: 0066-4146. DOI: 10.1146/annurev-astro-091918-104453. URL: <http://>

- //adsabs.harvard.edu/abs/2019ARA%26A..57..375S (visited on 04/22/2021).
- [32] Andrew Pontzen and Fabio Governato. “How supernova feedback turns dark matter cusps into cores”. In: *Monthly Notices of the Royal Astronomical Society* 421 (Apr. 2012), pp. 3464–3471. ISSN: 0035-8711. DOI: 10.1111/j.1365-2966.2012.20571.x. URL: <http://adsabs.harvard.edu/abs/2012MNRAS.421.3464P> (visited on 04/22/2021).
 - [33] T. K. Chan et al. “The impact of baryonic physics on the structure of dark matter haloes: the view from the FIRE cosmological simulations”. In: *Monthly Notices of the Royal Astronomical Society* 454 (Dec. 2015), pp. 2981–3001. ISSN: 0035-8711. DOI: 10.1093/mnras/stv2165. URL: <http://adsabs.harvard.edu/abs/2015MNRAS.454.2981C> (visited on 04/22/2021).
 - [34] David N. Spergel and Paul J. Steinhardt. “Observational Evidence for Self-Interacting Cold Dark Matter”. In: *Physical Review Letters* 84 (Apr. 2000), pp. 3760–3763. ISSN: 0031-9007. DOI: 10.1103/PhysRevLett.84.3760. URL: <http://adsabs.harvard.edu/abs/2000PhRvL..84.3760S> (visited on 04/22/2021).
 - [35] Andreas Burkert. “The Structure and Evolution of Weakly Self-interacting Cold Dark Matter Halos”. In: *The Astrophysical Journal Letters* 534 (May 2000), pp. L143–L146. ISSN: 0004-637X. DOI: 10.1086/312674. URL: <http://adsabs.harvard.edu/abs/2000ApJ...534L.143B> (visited on 04/23/2021).
 - [36] Romeel Davé et al. “Halo Properties in Cosmological Simulations of Self-interacting Cold Dark Matter”. In: *The Astrophysical Journal* 547 (Feb. 2001), pp. 574–589. ISSN: 0004-637X. DOI: 10.1086/318417. URL: <http://adsabs.harvard.edu/abs/2001ApJ...547..574D> (visited on 04/23/2021).
 - [37] Ben Moore et al. “Collisional versus Collisionless Dark Matter”. In: *The Astrophysical Journal Letters* 535 (May 2000), pp. L21–L24. ISSN:

- 0004-637X. DOI: 10.1086/312692. URL: <http://adsabs.harvard.edu/abs/2000ApJ...535L..21M> (visited on 04/23/2021).
- [38] Naoki Yoshida et al. “Collisional Dark Matter and the Structure of Dark Halos”. In: *The Astrophysical Journal Letters* 535 (June 2000), pp. L103–L106. ISSN: 0004-637X. DOI: 10.1086/312707. URL: <http://adsabs.harvard.edu/abs/2000ApJ...535L.103Y> (visited on 04/23/2021).
- [39] Naoki Yoshida et al. “Weakly Self-interacting Dark Matter and the Structure of Dark Halos”. In: *The Astrophysical Journal Letters* 544 (Dec. 2000), pp. L87–L90. ISSN: 0004-637X. DOI: 10.1086/317306. URL: <http://adsabs.harvard.edu/abs/2000ApJ...544L..87Y> (visited on 04/23/2021).
- [40] Massimo Meneghetti et al. “Giant cluster arcs as a constraint on the scattering cross-section of dark matter”. In: *Monthly Notices of the Royal Astronomical Society* 325 (July 2001), pp. 435–442. ISSN: 0035-8711. DOI: 10.1046/j.1365-8711.2001.04477.x. URL: <http://adsabs.harvard.edu/abs/2001MNRAS.325..435M> (visited on 04/23/2021).
- [41] Jordi Miralda-Escudé. “A Test of the Collisional Dark Matter Hypothesis from Cluster Lensing”. In: *The Astrophysical Journal* 564 (Jan. 2002), pp. 60–64. ISSN: 0004-637X. DOI: 10.1086/324138. URL: <http://adsabs.harvard.edu/abs/2002ApJ...564...60M> (visited on 04/23/2021).
- [42] Miguel Rocha et al. “Cosmological simulations with self-interacting dark matter - I. Constant-density cores and substructure”. In: *Monthly Notices of the Royal Astronomical Society* 430 (Mar. 2013), pp. 81–104. ISSN: 0035-8711. DOI: 10.1093/mnras/sts514. URL: <http://adsabs.harvard.edu/abs/2013MNRAS.430...81R> (visited on 04/23/2021).
- [43] Annika H. G. Peter et al. “Cosmological simulations with self-interacting dark matter - II. Halo shapes versus observations”. In: *Monthly No-*

- tices of the Royal Astronomical Society* 430 (Mar. 2013), pp. 105–120. ISSN: 0035-8711. DOI: 10.1093/mnras/sts535. URL: <http://adsabs.harvard.edu/abs/2013MNRAS.430..105P> (visited on 04/23/2021).
- [44] Jesús Zavala, Mark Vogelsberger, and Matthew G. Walker. “Constraining self-interacting dark matter with the Milky Way’s dwarf spheroidals”. In: *Monthly Notices of the Royal Astronomical Society* 431 (Apr. 2013), pp. L20–L24. ISSN: 0035-8711. DOI: 10.1093/mnrasl/sls053. URL: <http://adsabs.harvard.edu/abs/2013MNRAS.431L..20Z> (visited on 04/23/2021).
- [45] Oliver D. Elbert et al. “Core formation in dwarf haloes with self-interacting dark matter: no fine-tuning necessary”. In: *Monthly Notices of the Royal Astronomical Society* 453 (Oct. 2015), pp. 29–37. ISSN: 0035-8711. DOI: 10.1093/mnras/stv1470. URL: <http://adsabs.harvard.edu/abs/2015MNRAS.453...29E> (visited on 04/23/2021).
- [46] Sean Tulin and Hai-Bo Yu. “Dark matter self-interactions and small scale structure”. In: *Physics Reports* 730 (Feb. 2018), pp. 1–57. ISSN: 0370-1573. DOI: 10.1016/j.physrep.2017.11.004. URL: <http://adsabs.harvard.edu/abs/2018PhR...730....1T> (visited on 04/19/2021).
- [47] Sean Tulin, Hai-Bo Yu, and Kathryn M. Zurek. “Beyond Collisionless Dark Matter: Particle Physics Dynamics for Dark Matter Halo Structure”. In: *Phys. Rev. D* 87.11 (June 2013). arXiv: 1302.3898, p. 115007. ISSN: 1550-7998, 1550-2368. DOI: 10.1103/PhysRevD.87.115007. URL: <http://arxiv.org/abs/1302.3898> (visited on 01/05/2021).
- [48] Sean Tulin, Hai-Bo Yu, and Kathryn M. Zurek. “Resonant Dark Forces and Small Scale Structure”. In: *Phys. Rev. Lett.* 110.11 (Mar. 2013). arXiv: 1210.0900, p. 111301. ISSN: 0031-9007, 1079-7114. DOI: 10.1103/PhysRevLett.110.111301. URL: <http://arxiv.org/abs/1210.0900> (visited on 01/05/2021).

- [49] Graham D. Kribs and Ethan T. Neil. “Review of strongly-coupled composite dark matter models and lattice simulations”. In: *Int. J. Mod. Phys. A* 31.22 (Aug. 2016). arXiv: 1604.04627, p. 1643004. ISSN: 0217-751X, 1793-656X. DOI: 10 . 1142 / S0217751X16430041. URL: <http://arxiv.org/abs/1604.04627> (visited on 01/05/2021).
- [50] James M. Cline et al. “Composite strongly interacting dark matter”. In: *Phys. Rev. D* 90.1 (July 2014). arXiv: 1312.3325, p. 015023. ISSN: 1550-7998, 1550-2368. DOI: 10 . 1103 / PhysRevD . 90 . 015023. URL: <http://arxiv.org/abs/1312.3325> (visited on 01/05/2021).
- [51] Manoj Kaplinghat et al. “Tying Dark Matter to Baryons with Self-Interactions”. In: *Physical Review Letters* 113 (July 2014), p. 021302. ISSN: 0031-9007. DOI: 10 . 1103 / PhysRevLett . 113 . 021302. URL: <http://adsabs.harvard.edu/abs/2014PhRvL.113b1302K> (visited on 04/23/2021).
- [52] Philip F. Hopkins. “A new class of accurate, mesh-free hydrodynamic simulation methods”. In: *Monthly Notices of the Royal Astronomical Society* 450 (June 2015), pp. 53–110. ISSN: 0035-8711. DOI: 10 . 1093 / mnras/stv195. URL: <http://adsabs.harvard.edu/abs/2015MNRAS.450...53H> (visited on 04/23/2021).
- [53] R. A. Ibata, G. Gilmore, and M. J. Irwin. “A dwarf satellite galaxy in Sagittarius”. en. In: *Nature* 370.6486 (July 1994). Number: 6486 Publisher: Nature Publishing Group, pp. 194–196. ISSN: 1476-4687. DOI: 10 . 1038 / 370194a0. URL: <https://www.nature.com/articles/370194a0> (visited on 04/23/2021).
- [54] Ing-Guey Jiang and James Binney. “The orbit and mass of the Sagittarius dwarf galaxy”. In: *Monthly Notices of the Royal Astronomical Society* 314 (May 2000), pp. 468–474. ISSN: 0035-8711. DOI: 10 . 1046 / j . 1365 - 8711 . 2000 . 03311 . x. URL: <http://adsabs.harvard.edu/abs/2000MNRAS.314..468J> (visited on 04/23/2021).

- [55] Steven R. Majewski et al. “A Two Micron All Sky Survey View of the Sagittarius Dwarf Galaxy. I. Morphology of the Sagittarius Core and Tidal Arms”. In: *The Astrophysical Journal* 599 (Dec. 2003), pp. 1082–1115. ISSN: 0004-637X. DOI: 10.1086/379504. URL: <http://adsabs.harvard.edu/abs/2003ApJ...599.1082M> (visited on 04/23/2021).
- [56] V. Belokurov et al. “The Field of Streams: Sagittarius and Its Siblings”. In: *The Astrophysical Journal Letters* 642 (May 2006), pp. L137–L140. ISSN: 0004-637X. DOI: 10.1086/504797. URL: <http://adsabs.harvard.edu/abs/2006ApJ...642L.137B> (visited on 04/24/2021).
- [57] Andrea Kunder and Brian Chaboyer. “Distance to the Sagittarius Dwarf Galaxy Using Macho Project RR Lyrae Stars”. In: *The Astronomical Journal* 137 (May 2009), pp. 4478–4486. ISSN: 0004-6256. DOI: 10.1088/0004-6256/137/5/4478. URL: <http://adsabs.harvard.edu/abs/2009AJ....137.4478K> (visited on 04/23/2021).
- [58] David R. Law and Steven R. Majewski. “The Sagittarius Dwarf Galaxy: A Model for Evolution in a Triaxial Milky Way Halo”. In: *The Astrophysical Journal* 714 (May 2010), pp. 229–254. ISSN: 0004-637X. DOI: 10.1088/0004-637X/714/1/229. URL: <http://adsabs.harvard.edu/abs/2010ApJ...714..229L> (visited on 04/23/2021).
- [59] Marion Dierickx and Abraham Loeb. “Predicted Extension of the Sagittarius Stream to the Milky Way Virial Radius”. In: *ApJ* 836.1 (Feb. 2017). arXiv: 1611.00089, p. 92. ISSN: 1538-4357. DOI: 10.3847/1538-4357/836/1/92. URL: <http://arxiv.org/abs/1611.00089> (visited on 09/13/2020).
- [60] Chris W. Purcell et al. “The Sagittarius impact as an architect of spirality and outer rings in the Milky Way”. In: *Nature* 477 (Sept. 2011), pp. 301–303. ISSN: 0028-0836. DOI: 10.1038/nature10417. URL: <http://adsabs.harvard.edu/abs/2011Natur.477..301P> (visited on 04/23/2021).

- [61] N. Deg et al. “GalactICS with Gas”. In: *Monthly Notices of the Royal Astronomical Society* 486.4 (July 2019). arXiv: 1904.12700, pp. 5391–5399. ISSN: 0035-8711, 1365-2966. DOI: 10.1093/mnras/stz1203. URL: <http://arxiv.org/abs/1904.12700> (visited on 01/05/2021).
- [62] Lawrence M. Widrow, Brent Pym, and John Dubinski. “Dynamical Blueprints for Galaxies”. In: *ApJ* 679.2 (June 2008). arXiv: 0801.3414, pp. 1239–1259. ISSN: 0004-637X, 1538-4357. DOI: 10.1086/587636. URL: <http://arxiv.org/abs/0801.3414> (visited on 01/07/2021).
- [63] Volker Springel. “The cosmological simulation code GADGET-2”. In: *Monthly Notices of the Royal Astronomical Society* 364.4 (Dec. 2005). arXiv: astro-ph/0505010, pp. 1105–1134. ISSN: 0035-8711, 1365-2966. DOI: 10.1111/j.1365-2966.2005.09655.x. URL: <http://arxiv.org/abs/astro-ph/0505010> (visited on 01/05/2021).
- [64] Princeton Research Computing. *Della*. en. URL: <https://researchcomputing.princeton.edu/systems/della> (visited on 04/25/2021).
- [65] NASA and California Institute of Technology. *NASA/IPAC Extragalactic Database: Sagittarius Dwarf Spheroidal*. URL: http://ned.ipac.caltech.edu/cgi-bin/objsearch?search_type=Obj_id&objid=326262&objname=1&img_stamp=YES&hconst=73.0&omegam=0.27&omegav=0.73&corr_z=1.
- [66] D. Massari et al. “Hubble Space Telescope Absolute Proper Motions of NGC 6681 (M70) and the Sagittarius Dwarf Spheroidal Galaxy”. In: *ApJ* 779.1 (Nov. 2013), p. 81. ISSN: 0004-637X, 1538-4357. DOI: 10.1088/0004-637X/779/1/81. URL: <https://iopscience.iop.org/article/10.1088/0004-637X/779/1/81> (visited on 01/07/2021).
- [67] M. Bellazzini et al. “The Nucleus of the Sagittarius dSph Galaxy and M54: A Window on the Process of Galaxy Nucleation”. In: *The Astronomical Journal* 136.3 (Sept. 2008), pp. 1147–1170. ISSN: 0004-6256, 1538-3881. DOI: 10.1088/0004-6256/136/3/1147. URL: <https://iopscience.iop.org/article/10.1088/0004-6256/136/3/1147> :

- //iopscience.iop.org/article/10.1088/0004-6256/136/3/1147 (visited on 01/07/2021).
- [68] L. Lindegren et al. “Gaia Data Release 2. The astrometric solution”. In: *Astronomy and Astrophysics* 616 (Aug. 2018), A2. ISSN: 0004-6361. DOI: 10.1051/0004-6361/201832727. URL: [http://adsabs.harvard.edu/abs/2018A%26A...616A...2L](http://adsabs.harvard.edu/abs/2018A<26A...616A...2L) (visited on 04/27/2021).
 - [69] Gaia Collaboration et al. “Gaia Data Release 2. Summary of the contents and survey properties”. In: *Astronomy and Astrophysics* 616 (Aug. 2018), A1. ISSN: 0004-6361. DOI: 10.1051/0004-6361/201833051. URL: [http://adsabs.harvard.edu/abs/2018A%26A...616A...1G](http://adsabs.harvard.edu/abs/2018A<26A...616A...1G) (visited on 04/27/2021).
 - [70] Rodrigo Ibata et al. “A Panoramic Landscape of the Sagittarius Stream in Gaia DR2 Revealed with the STREAMFINDER Spyglass”. In: *The Astrophysical Journal Letters* 891 (Mar. 2020), p. L19. ISSN: 0004-637X. DOI: 10.3847/2041-8213/ab77c7. URL: <http://adsabs.harvard.edu/abs/2020ApJ...891L..19I> (visited on 04/27/2021).
 - [71] Khyati Malhan and Rodrigo A Ibata. “STREAMFINDER – I. A new algorithm for detecting stellar streams”. In: *Monthly Notices of the Royal Astronomical Society* 477.3 (July 2018), pp. 4063–4076. ISSN: 0035-8711. DOI: 10.1093/mnras/sty912. URL: <https://doi.org/10.1093/mnras/sty912> (visited on 04/27/2021).
 - [72] Khyati Malhan, Rodrigo A Ibata, and Nicolas F Martin. “Ghostly tributaries to the Milky Way: charting the halo’s stellar streams with the Gaia DR2 catalogue”. In: *Monthly Notices of the Royal Astronomical Society* 481.3 (Dec. 2018), pp. 3442–3455. ISSN: 0035-8711. DOI: 10.1093/mnras/sty2474. URL: <https://doi.org/10.1093/mnras/sty2474> (visited on 04/27/2021).
 - [73] Astropy Collaboration et al. “Astropy: A community Python package for astronomy”. In: *Astronomy and Astrophysics* 558 (Oct. 2013), A33. ISSN: 0004-6361. DOI: 10.1051/0004-6361/201322068. URL: <http://>

- //adsabs.harvard.edu/abs/2013A%26A...558A..33A (visited on 04/27/2021).
- [74] Astropy Collaboration et al. “The Astropy Project: Building an Open-science Project and Status of the v2.0 Core Package”. In: *The Astronomical Journal* 156 (Sept. 2018), p. 123. ISSN: 0004-6256. DOI: 10.3847/1538-3881/aabc4f. URL: <http://adsabs.harvard.edu/abs/2018AJ....156..123A> (visited on 04/27/2021).